

Measurements of directed, elliptic, and triangular flow in Cu + Au collisions at $\sqrt{s_{NN}}=200$ GeV

(PHENIX Collaboration) Adare, A.; ...; Makek, Mihael; ...; Zou, L.

Source / Izvornik: **Physical Review C, 2016, 94**

Journal article, Published version

Rad u časopisu, Objavljena verzija rada (izdavačev PDF)

<https://doi.org/10.1103/PhysRevC.94.054910>

Permanent link / Trajna poveznica: <https://um.nsk.hr/um:nbn:hr:217:726786>

Rights / Prava: [In copyright](#) / [Zaštićeno autorskim pravom.](#)

Download date / Datum preuzimanja: **2024-11-18**



Repository / Repozitorij:

[Repository of the Faculty of Science - University of Zagreb](#)



Measurements of directed, elliptic, and triangular flow in Cu + Au collisions at $\sqrt{s_{NN}} = 200$ GeV

A. Adare,¹³ C. Aidala,^{38,42} N. N. Ajitanand,⁶⁰ Y. Akiba,^{55,56} R. Akimoto,¹² J. Alexander,⁶⁰ M. Alfred,²² K. Aoki,^{31,55} N. Apadula,^{27,61} H. Asano,^{34,55} E. T. Atomssa,⁶¹ T. C. Awes,⁵¹ B. Azmoun,⁷ V. Babintsev,²³ M. Bai,⁶ X. Bai,¹¹ N. S. Bandara,⁴¹ B. Bannier,⁶¹ K. N. Barish,⁸ S. Bathe,^{5,56} V. Baublis,⁵⁴ C. Baumann,⁷ S. Baumgart,⁵⁵ A. Bazilevsky,⁷ M. Beaumier,⁸ S. Beckman,¹³ R. Belmont,^{13,42,66} A. Berdnikov,⁵⁸ Y. Berdnikov,⁵⁸ D. Black,⁸ D. S. Blau,³³ J. S. Bok,⁴⁹ K. Boyle,⁵⁶ M. L. Brooks,³⁸ J. Bryslawski,^{5,8} H. Buesching,⁷ V. Bumazhnov,²³ S. Butsyk,⁴⁸ S. Campbell,^{14,27} C.-H. Chen,⁵⁶ C. Y. Chi,¹⁴ M. Chiu,⁷ I. J. Choi,²⁴ J. B. Choi,^{10,*} S. Choi,⁵⁹ P. Christiansen,³⁹ T. Chujo,⁶⁵ V. Ciaciolo,⁵¹ Z. Citron,⁶⁷ B. A. Cole,¹⁴ N. Cronin,^{42,61} N. Crossette,⁴³ M. Csanád,¹⁶ T. Csörgő,⁶⁸ T. W. Danley,⁵⁰ A. Datta,⁴⁸ M. S. Daugherty,¹ G. David,⁷ K. DeBlasio,⁴⁸ K. Dehmelt,⁶¹ A. Denisov,²³ A. Deshpande,^{56,61} E. J. Desmond,⁷ L. Ding,²⁷ A. Dion,⁶¹ P. B. Diss,⁴⁰ J. H. Do,⁶⁹ L. D’Orazio,⁴⁰ O. Drapier,³⁵ A. Drees,⁶¹ K. A. Drees,⁶ J. M. Durham,³⁸ A. Durum,²³ T. Engelmöore,¹⁴ A. Enokizono,^{55,57} S. Esumi,⁶⁵ K. O. Eyster,⁷ B. Fadern,⁴³ N. Feege,⁶¹ D. E. Fields,⁴⁸ M. Finger,⁹ M. Finger, Jr.,⁹ F. Fleuret,³⁵ S. L. Fokin,³³ J. E. Frantz,⁵⁰ A. Franz,⁷ A. D. Frawley,¹⁸ Y. Fukao,³¹ T. Fusayasu,⁴⁵ K. Gainey,¹ C. Gal,⁶¹ P. Gallus,¹⁵ P. Garg,³ A. Garishvili,⁶³ I. Garishvili,³⁷ H. Ge,⁶¹ F. Giordano,²⁴ A. Glenn,³⁷ X. Gong,⁶⁰ M. Gonin,³⁵ Y. Goto,^{55,56} R. Granier de Cassagnac,³⁵ N. Grau,² S. V. Greene,⁶⁶ M. Grosse Perdekamp,²⁴ Y. Gu,⁶⁰ T. Gunji,¹² H. Guragain,¹⁹ T. Hachiya,^{55,56} J. S. Haggerty,⁷ K. I. Hahn,¹⁷ H. Hamagaki,¹² H. F. Hamilton,¹ S. Y. Han,¹⁷ J. Hanks,⁶¹ S. Hasegawa,²⁸ T. O. S. Haseler,¹⁹ K. Hashimoto,^{55,57} R. Hayano,¹² X. He,¹⁹ T. K. Hemmick,⁶¹ T. Hester,⁸ J. C. Hill,²⁷ R. S. Hollis,⁸ K. Homma,²¹ B. Hong,³² T. Hoshino,²¹ N. Hotvedt,²⁷ J. Huang,^{7,38} S. Huang,⁶⁶ T. Ichihara,^{55,56} Y. Ikeda,⁵⁵ K. Imai,²⁸ Y. Imazu,⁵⁵ M. Inaba,⁶⁵ A. Iordanova,⁸ D. Isenhower,¹ A. Isinhue,⁴³ D. Ivanishchev,⁵⁴ B. V. Jacak,⁶¹ S. J. Jeon,⁴⁴ M. Jezghani,¹⁹ J. Jia,^{7,60} X. Jiang,³⁸ B. M. Johnson,^{7,19} K. S. Joo,⁴⁴ D. Jouan,⁵² D. S. Jumper,²⁴ J. Kamin,⁶¹ S. Kanda,^{12,31} B. H. Kang,²⁰ J. H. Kang,⁶⁹ J. S. Kang,²⁰ J. Kapustinsky,³⁸ D. Kawall,⁴¹ A. V. Kazantsev,³³ J. A. Key,⁴⁸ V. Khachatryan,⁶¹ P. K. Khandai,³ A. Khanzadeev,⁵⁴ K. M. Kijima,²¹ C. Kim,³² D. J. Kim,²⁹ E.-J. Kim,¹⁰ G. W. Kim,¹⁷ M. Kim,⁵⁹ Y.-J. Kim,²⁴ Y. K. Kim,²⁰ B. Kimelman,⁴³ E. Kistenev,⁷ R. Kitamura,¹² J. Klatsky,¹⁸ D. Kleinjan,⁸ P. Kline,⁶¹ T. Koblesky,¹³ M. Kofarago,¹⁶ B. Komkov,⁵⁴ J. Koster,⁵⁶ D. Kotchetkov,⁵⁰ D. Kotov,^{54,58} F. Krizek,²⁹ K. Kurita,⁵⁷ M. Kurosawa,^{55,56} Y. Kwon,⁶⁹ R. Lacey,⁶⁰ Y. S. Lai,¹⁴ J. G. Lajoie,²⁷ A. Lebedev,²⁷ D. M. Lee,³⁸ G. H. Lee,¹⁰ J. Lee,^{17,62} K. B. Lee,³⁸ K. S. Lee,³² S. Lee,⁶⁹ S. H. Lee,⁶¹ M. J. Leitch,³⁸ M. Leitgab,²⁴ B. Lewis,⁶¹ X. Li,¹¹ S. H. Lim,⁶⁹ M. X. Liu,³⁸ D. Lynch,⁷ C. F. Maguire,⁶⁶ Y. I. Makdisi,⁶ M. Makek,^{67,70} A. Manion,⁶¹ V. I. Manko,³³ E. Mannel,⁷ T. Maruyama,²⁸ M. McCumber,^{13,38} P. L. McGaughey,³⁸ D. McGlinchey,^{13,18} C. McKinney,²⁴ A. Meles,⁴⁹ M. Mendoza,⁸ B. Meredith,²⁴ Y. Miake,⁶⁵ T. Mibe,³¹ A. C. Mignerey,⁴⁰ A. Milov,⁶⁷ D. K. Mishra,⁴ J. T. Mitchell,⁷ S. Miyasaka,^{55,64} S. Mizuno,^{55,65} A. K. Mohanty,⁴ S. Mohapatra,⁶⁰ P. Montuenga,²⁴ T. Moon,⁶⁹ D. P. Morrison,^{7,†} M. Moskowitza,⁴⁰ T. V. Moukhanova,³³ T. Murakami,^{34,55} J. Murata,^{55,57} A. Mwai,⁶⁰ T. Nagae,³⁴ S. Nagamiya,^{31,55} K. Nagashima,²¹ J. L. Nagle,^{13,‡} M. I. Nagy,¹⁶ I. Nakagawa,^{55,56} H. Nakagomi,^{55,65} Y. Nakamiya,²¹ K. R. Nakamura,^{34,55} T. Nakamura,⁵⁵ K. Nakano,^{55,64} C. Nattrass,⁶³ P. K. Netrakanti,⁴ M. Nihashi,^{21,55} T. Niida,⁶⁵ S. Nishimura,¹² R. Nouicer,^{7,56} T. Novák,^{30,68} N. Novitzky,^{29,61} A. S. Nyanin,³³ E. O’Brien,⁷ C. A. Ogilvie,²⁷ H. Oide,¹² K. Okada,⁵⁶ J. D. Orjuela Koop,¹³ J. D. Osborn,⁴² A. Oskarsson,³⁹ K. Ozawa,³¹ R. Pak,⁷ V. Pantuev,²⁵ V. Papavassiliou,⁴⁹ I. H. Park,^{17,62} J. S. Park,⁵⁹ S. Park,⁵⁹ S. K. Park,³² S. F. Pate,⁴⁹ L. Patel,¹⁹ M. Patel,²⁷ J.-C. Peng,²⁴ D. V. Perepelitsa,^{7,13,14} G. D. N. Perera,⁴⁹ D. Yu. Peressouko,³³ J. Perry,²⁷ R. Petti,^{7,61} C. Pinkenburg,⁷ R. Pinson,¹ R. P. Pisani,⁷ M. L. Purschke,⁷ H. Qu,¹ J. Rak,²⁹ B. J. Ramson,⁴² I. Ravinovich,⁶⁷ K. F. Read,^{51,63} D. Reynolds,⁶⁰ V. Riabov,^{47,54} Y. Riabov,^{54,58} E. Richardson,⁴⁰ T. Rinn,²⁷ N. Rivieli,⁵⁰ D. Roach,⁶⁶ S. D. Rolnick,⁸ M. Rosati,²⁷ Z. Rowan,⁵ J. G. Rubin,⁴² M. S. Ryu,²⁰ B. Sahlmueller,⁶¹ N. Saito,³¹ T. Sakaguchi,⁷ H. Sako,²⁸ V. Samsonov,^{47,54} M. Sarsour,¹⁹ S. Sato,²⁸ S. Sawada,³¹ B. Schaefer,⁶⁶ B. K. Schmoll,⁶³ K. Sedgwick,⁸ J. Seele,⁵⁶ R. Seidl,^{55,56} Y. Sekiguchi,¹² A. Sen,^{19,27,63} R. Seto,⁸ P. Sett,⁴ A. Sexton,⁴⁰ D. Sharma,⁶¹ A. Shaver,²⁷ I. Shein,²³ T.-A. Shibata,^{55,64} K. Shigaki,²¹ M. Shimomura,^{27,46} K. Shoji,⁵⁵ P. Shukla,⁴ A. Sickles,^{7,24} C. L. Silva,³⁸ D. Silvermyr,^{39,51} B. K. Singh,³ C. P. Singh,³ V. Singh,³ M. Skolnik,⁴³ M. Slunečka,⁹ M. Snowball,³⁸ S. Solano,⁴³ R. A. Soltz,³⁷ W. E. Sondheim,³⁸ S. P. Sorensen,⁶³ I. V. Sourikova,⁷ P. W. Stankus,⁵¹ P. Steinberg,⁷ E. Stenlund,³⁹ M. Stepanov,^{41,*} A. Ster,⁶⁸ S. P. Stoll,⁷ M. R. Stone,¹³ T. Sugitate,²¹ A. Sukhanov,⁷ T. Sumita,⁵⁵ J. Sun,⁶¹ J. Sziklai,⁶⁸ A. Takahara,¹² A. Taketani,^{55,56} Y. Tanaka,⁴⁵ K. Tanida,^{56,59} M. J. Tannenbaum,⁷ S. Tarafdar,^{3,66,67} A. Taranenko,^{47,60} E. Tennant,⁴⁹ R. Tieulent,¹⁹ A. Timilsina,²⁷ T. Todoroki,^{55,65} M. Tomášek,^{15,26} H. Torii,¹² C. L. Towell,¹ R. Towell,¹ R. S. Towell,¹ I. Tserruya,⁶⁷ H. W. van Hecke,³⁸ M. Vargyas,¹⁶ E. Vazquez-Zambrano,¹⁴ A. Veicht,¹⁴ J. Velkovska,⁶⁶ R. Vértési,⁶⁸ M. Virius,¹⁵ V. Vrba,^{15,26} E. Vznuzdaev,⁵⁴ X. R. Wang,^{49,56} D. Watanabe,²¹ K. Watanabe,^{55,57} Y. Watanabe,^{55,56} Y. S. Watanabe,^{12,31} F. Wei,⁴⁹ S. Whitaker,²⁷ A. S. White,⁴² S. Wolin,²⁴ C. L. Woody,⁷ M. Wysocki,⁵¹ B. Xia,⁵⁰ L. Xue,¹⁹ S. Yalcin,⁶¹ Y. L. Yamaguchi,^{12,61} A. Yanovich,²³ S. Yokkaichi,^{55,56} J. H. Yoo,³² I. Yoon,⁵⁹ Z. You,³⁸ I. Younus,^{36,48} H. Yu,^{49,53} I. E. Yushmanov,³³ W. A. Zajc,¹⁴ A. Zelenski,⁶ S. Zhou,¹¹ and L. Zou⁸

(PHENIX Collaboration)

¹Abilene Christian University, Abilene, Texas 79699, USA²Department of Physics, Augustana University, Sioux Falls, South Dakota 57197, USA³Department of Physics, Banaras Hindu University, Varanasi 221005, India⁴Bhabha Atomic Research Centre, Bombay 400 085, India⁵Baruch College, City University of New York, New York, New York, 10010 USA⁶Collider-Accelerator Department, Brookhaven National Laboratory, Upton, New York 11973-5000, USA

- ⁷Physics Department, Brookhaven National Laboratory, Upton, New York 11973-5000, USA
- ⁸University of California-Riverside, Riverside, California 92521, USA
- ⁹Charles University, Ovocný trh 5, Praha 1, 116 36, Prague, Czech Republic
- ¹⁰Chonbuk National University, Jeonju, 561-756, Korea
- ¹¹Science and Technology on Nuclear Data Laboratory, China Institute of Atomic Energy, Beijing 102413, People's Republic of China
- ¹²Center for Nuclear Study, Graduate School of Science, University of Tokyo, 7-3-1 Hongo, Bunkyo, Tokyo 113-0033, Japan
- ¹³University of Colorado, Boulder, Colorado 80309, USA
- ¹⁴Columbia University, New York, New York 10027, USA
and Nevis Laboratories, Irvington, New York 10533, USA
- ¹⁵Czech Technical University, Zikova 4, 166 36 Prague 6, Czech Republic
- ¹⁶ELTE, Eötvös Loránd University, H-1117 Budapest, Pázmány P. s. 1/A, Hungary
- ¹⁷Ewha Womans University, Seoul 120-750, Korea
- ¹⁸Florida State University, Tallahassee, Florida 32306, USA
- ¹⁹Georgia State University, Atlanta, Georgia 30303, USA
- ²⁰Hanyang University, Seoul 133-792, Korea
- ²¹Hiroshima University, Kagamiyama, Higashi-Hiroshima 739-8526, Japan
- ²²Department of Physics and Astronomy, Howard University, Washington, D.C. 20059, USA
- ²³IHEP Protvino, State Research Center of Russian Federation, Institute for High Energy Physics, Protvino, 142281, Russia
- ²⁴University of Illinois at Urbana-Champaign, Urbana, Illinois 61801, USA
- ²⁵Institute for Nuclear Research of the Russian Academy of Sciences, prospekt 60-letiya Oktyabrya 7a, Moscow 117312, Russia
- ²⁶Institute of Physics, Academy of Sciences of the Czech Republic, Na Slovance 2, 182 21 Prague 8, Czech Republic
- ²⁷Iowa State University, Ames, Iowa 50011, USA
- ²⁸Advanced Science Research Center, Japan Atomic Energy Agency, 2-4 Shirakata Shirane, Tokai-mura, Naka-gun, Ibaraki-ken 319-1195, Japan
- ²⁹Helsinki Institute of Physics and University of Jyväskylä, P.O.Box 35, FI-40014 Jyväskylä, Finland
- ³⁰Károly Róberts University College, H-3200 Gynögyös, Mátrai út 36, Hungary
- ³¹KEK, High Energy Accelerator Research Organization, Tsukuba, Ibaraki 305-0801, Japan
- ³²Korea University, Seoul, 136-701, Korea
- ³³National Research Center "Kurchatov Institute," Moscow, 123098 Russia
- ³⁴Kyoto University, Kyoto 606-8502, Japan
- ³⁵Laboratoire Leprince-Ringuet, Ecole Polytechnique, CNRS-IN2P3, Route de Saclay, F-91128, Palaiseau, France
- ³⁶Physics Department, Lahore University of Management Sciences, Lahore 54792, Pakistan
- ³⁷Lawrence Livermore National Laboratory, Livermore, California 94550, USA
- ³⁸Los Alamos National Laboratory, Los Alamos, New Mexico 87545, USA
- ³⁹Department of Physics, Lund University, Box 118, SE-221 00 Lund, Sweden
- ⁴⁰University of Maryland, College Park, Maryland 20742, USA
- ⁴¹Department of Physics, University of Massachusetts, Amherst, Massachusetts 01003-9337, USA
- ⁴²Department of Physics, University of Michigan, Ann Arbor, Michigan 48109-1040, USA
- ⁴³Muhlenberg College, Allentown, Pennsylvania 18104-5586, USA
- ⁴⁴Myongji University, Yongin, Kyonggido 449-728, Korea
- ⁴⁵Nagasaki Institute of Applied Science, Nagasaki-shi, Nagasaki 851-0193, Japan
- ⁴⁶Nara Women's University, Kita-uoya Nishi-machi Nara 630-8506, Japan
- ⁴⁷National Research Nuclear University, MEPhI, Moscow Engineering Physics Institute, Moscow, 115409, Russia
- ⁴⁸University of New Mexico, Albuquerque, New Mexico 87131, USA
- ⁴⁹New Mexico State University, Las Cruces, New Mexico 88003, USA
- ⁵⁰Department of Physics and Astronomy, Ohio University, Athens, Ohio 45701, USA
- ⁵¹Oak Ridge National Laboratory, Oak Ridge, Tennessee 37831, USA
- ⁵²IPN-Orsay, Université Paris-Sud, CNRS/IN2P3, Université Paris-Saclay, BPI, F-91406, Orsay, France
- ⁵³Peking University, Beijing 100871, People's Republic of China
- ⁵⁴PNPI, Petersburg Nuclear Physics Institute, Gatchina, Leningrad region, 188300, Russia
- ⁵⁵RIKEN Nishina Center for Accelerator-Based Science, Wako, Saitama 351-0198, Japan
- ⁵⁶RIKEN BNL Research Center, Brookhaven National Laboratory, Upton, New York 11973-5000, USA
- ⁵⁷Physics Department, Rikkyo University, 3-34-1 Nishi-Ikebukuro, Toshima, Tokyo 171-8501, Japan
- ⁵⁸Saint Petersburg State Polytechnic University, St. Petersburg, 195251 Russia
- ⁵⁹Department of Physics and Astronomy, Seoul National University, Seoul 151-742, Korea
- ⁶⁰Chemistry Department, Stony Brook University, SUNY, Stony Brook, New York 11794-3400, USA
- ⁶¹Department of Physics and Astronomy, Stony Brook University, SUNY, Stony Brook, New York 11794-3800, USA
- ⁶²Sungkyunkwan University, Suwon, 440-746, Korea
- ⁶³University of Tennessee, Knoxville, Tennessee 37996, USA

⁶⁴*Department of Physics, Tokyo Institute of Technology, Oh-okayama, Meguro, Tokyo 152-8551, Japan*

⁶⁵*Center for Integrated Research in Fundamental Science and Engineering, University of Tsukuba, Tsukuba, Ibaraki 305, Japan*

⁶⁶*Vanderbilt University, Nashville, Tennessee 37235, USA*

⁶⁷*Weizmann Institute, Rehovot 76100, Israel*

⁶⁸*Institute for Particle and Nuclear Physics, Wigner Research Centre for Physics, Hungarian Academy of Sciences (Wigner RCP, RMKI)*

H-1525 Budapest 114, POBox 49, Budapest, Hungary

⁶⁹*Yonsei University, IPAP, Seoul 120-749, Korea*

⁷⁰*University of Zagreb, Faculty of Science, Department of Physics, Bijenička 32, HR-10002 Zagreb, Croatia*

(Received 5 October 2015; revised manuscript received 4 October 2016; published 28 November 2016)

Measurements of anisotropic flow Fourier coefficients (v_n) for inclusive charged particles and identified hadrons π^\pm , K^\pm , p , and \bar{p} produced at midrapidity in Cu + Au collisions at $\sqrt{s_{NN}} = 200$ GeV are presented. The data were collected in 2012 by the PHENIX experiment at the Relativistic Heavy-Ion Collider (RHIC). The particle azimuthal distributions with respect to different-order symmetry planes Ψ_n , for $n = 1, 2$, and 3 are studied as a function of transverse momentum p_T over a broad range of collision centralities. Mass ordering, as expected from hydrodynamic flow, is observed for all three harmonics. The charged-particle results are compared with hydrodynamical and transport model calculations. We also compare these Cu + Au results with those in Cu + Cu and Au + Au collisions at the same $\sqrt{s_{NN}}$ and find that the v_2 and v_3 , as a function of transverse momentum, follow a common scaling with $1/(\varepsilon_n N_{\text{part}}^{1/3})$.

DOI: [10.1103/PhysRevC.94.054910](https://doi.org/10.1103/PhysRevC.94.054910)

I. INTRODUCTION

Measurements of azimuthal anisotropies of particle emission in relativistic heavy-ion collisions have proven to be an essential tool in probing the properties of the quark gluon plasma (QGP) produced in such collisions. These anisotropies can be quantified [1] by the coefficients v_n in the Fourier expansion of the particle distributions with respect to symmetry planes of the same-order Ψ_n that are determined on an event-by-event basis: $dN/d\phi \propto 1 + \sum_{n=1} 2v_n \cos[n(\phi - \Psi_n)]$, where n is the order of the harmonic, ϕ is the azimuthal angle of particles of a given type, and Ψ_n is the azimuthal angle of the n th-order symmetry plane. Measurements of the second harmonic, which indicates the strength of the “elliptic flow,” led to the conclusion that the QGP produced at RHIC behaves as a nearly inviscid fluid [2–6]. In the last decade, significant effort, both experimentally and theoretically, has gone towards quantifying the specific viscosity η/s (shear viscosity over entropy density) of the produced QGP, as well as its temperature dependence.

Elliptic flow is thought to arise from the initial spatial anisotropy in the nuclear overlap zone, which has a lenticular shape in off-center nucleus-nucleus ($A + A$) collisions. This spatial anisotropy is then converted to a momentum-space anisotropy through the pressure gradients in the expanding fluid. Measurements of v_2 have been performed in symmetric $A + A$ collision for a variety of collision energies and particle species as a function of transverse momentum, rapidity, and system size [7–15]. Various scaling properties have been explored with the goal of understanding the onset of QGP formation with center-of-mass energy and how its properties may vary. The elliptic flow scaled by the corresponding initial spatial eccentricity (ε_2) was found to follow a universal trend

when plotted against the produced particle density in the transverse plane [8,9,15] over a broad range of center-of-mass energies. In a more recent study [12], PHENIX showed that the transverse particle density is proportional to the third root of the number of participant nucleons $N_{\text{part}}^{1/3}$ and that scaling with $(\varepsilon_2 N_{\text{part}}^{1/3})$ removes the remaining system-size dependencies at various center-of-mass energies.

The first-order Fourier coefficient v_1 , which is a measure of the strength of the “directed flow,” has also been studied in symmetric $A + A$ collisions over a broad range of energies [7,8,16–18]. Most studies focus on measurements of p_T -integrated values of v_1 as a function of rapidity or pseudorapidity, and the slope of dv_1/dy at midrapidity, which may yield information on the location of a first-order phase transition in the phase diagram of nuclear matter [19]. In symmetric $A + A$ collisions, if the nuclei are considered to be smooth spheres, v_1 is an odd function with respect to (pseudo)rapidity and vanishes at midrapidity, which is consistent with the p_T -integrated measurements.

Indeed, when the nuclei are taken as smooth spheres, all odd harmonics should vanish at midrapidity. However, event-by-event fluctuations in the initial geometry can lead to nonzero odd harmonics at midrapidity [20]. Sizable values for these harmonics have been measured at both RHIC (v_3) [21–23] and the Large Hadron Collider (v_3 and v_5) [24–26]. Evidence for a small rapidity-even component of v_1 at midrapidity has also been observed [18]. The combined experimental information from odd and even flow harmonics provides much more stringent constraints on the theoretical models [27–32] and the extracted QGP properties than measurements of elliptic flow alone.

Despite the wealth of experimental data and theoretical studies, uncertainties in the energy density deposition in the initial state of the heavy-ion collisions remain a limiting factor in deducing the specific viscosity of the QGP. Asymmetric collision systems, such as Cu + Au, provide opportunities

*Deceased.

[†]PHENIX Co-spokesperson: morrison@bnl.gov

[‡]PHENIX Co-spokesperson: jamie.nagle@colorado.edu

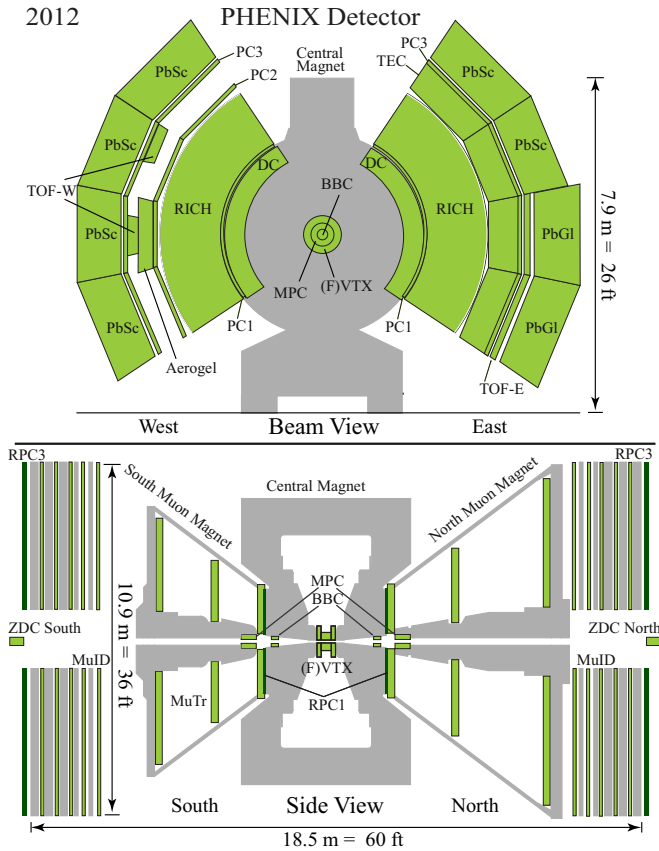


FIG. 1. The PHENIX detector configuration for RHIC Run-12 data-taking period

to study the effect of the initial geometry on the collective flow, particularly because odd harmonics may be enhanced at midrapidity beyond the fluctuation effects.

In this paper, we present measurements of v_1 , v_2 , and v_3 of charged particles and identified hadrons π^\pm , K^\pm , p , and \bar{p} produced at midrapidity in Cu + Au collisions at $\sqrt{s_{NN}} = 200$ GeV. In Sec. II we present the experimental details of the measurements, and the sources of systematic uncertainties. The results of the measurements are presented in Sec. III. In Sec. III C we compare the flow results obtained in different collision systems and explore their scaling behavior,

and in Sec. III D we present comparisons with theoretical calculations. Section IV summarizes our findings.

II. EXPERIMENTAL DETAILS

The PHENIX experiment is designed for the study of nuclear matter in extreme conditions by using a wide variety of experimental observables. The detector, optimized for the high-multiplicity environment of ultrarelativistic heavy-ion collisions, comprises two central-arm spectrometers (east and west), two muon spectrometers (at forward and backward rapidity), and a set of detectors used to determine the global properties of the collisions. Figure 1 shows a schematic diagram of the PHENIX detector for the data recorded in 2012. The upper drawing shows a beam-axis view of the two central spectrometer arms, covering the pseudorapidity region $|\eta| < 0.35$. The lower drawing shows a side view of the two forward-rapidity muon arms (north and south) and the global detectors. A detailed description of the complete set of detectors is given in Ref. [33].

The analysis presented here employs the global detectors, drift chamber (DC), three layers of multiwire proportional chambers (PC1, PC2, and PC3), the time-of-flight detectors (TOFE, TOFW), and the electromagnetic calorimeter (EM-Cal). The global system includes the beam-beam counters (BBCs), zero-degree calorimeters (ZDCs) and the shower maximum detectors (SMDs). Below, we give a brief description of each of these detector subsystems and their role in the present analysis.

A. Global detectors

The BBCs are located at ± 144 cm from the nominal interaction point along the beam line, cover 2π in azimuth, and span the pseudorapidity range $3.0 < |\eta| < 3.9$. Each BBC comprises 64 Čerenkov telescopes, arranged radially around the beam line. The BBCs provide the main interaction trigger for the experiment and are also used in the determination of the collision vertex position along the beam axis (z vertex) with $\sigma_z = 0.6$ cm resolution and the centrality of the collisions. The event centrality class in Cu + Au collisions is determined as a percentile of the total charge measured in the BBC from both sides. The BBCs also provide the

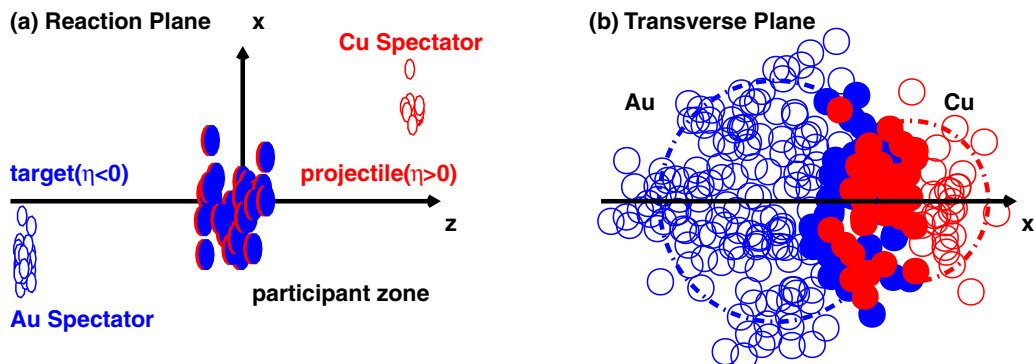


FIG. 2. Sketch of a noncentral heavy-ion collision. See text for description of the figure.

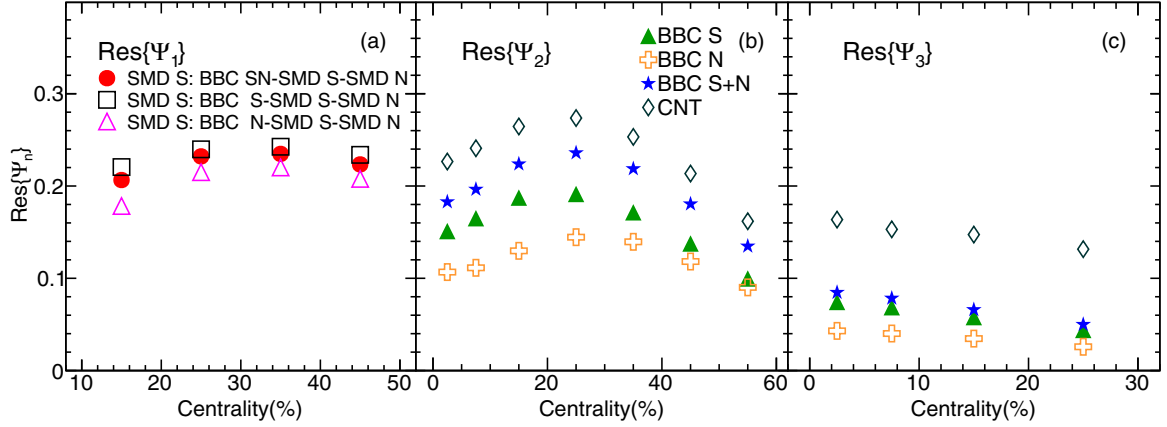


FIG. 3. (a) Event-plane resolution as a function of centrality for the SMDS detectors. (b), (c) Second- and third-order event-plane resolution. The BBC event-plane resolution is obtained from two subevents and BBCS, BBCN, CNT from three subevents as a function of centrality.

start time for the time-of-flight measurement with a timing resolution around $\sigma_t = 40$ ps in central Cu + Au collisions [33].

The ZDCs [34] are hadronic calorimeters located forward and backward of the PHENIX detector, along the beam line. Each ZDC is subdivided into three identical modules of two interaction lengths. They cover a pseudorapidity range of $|\eta| > 6.5$ and measure the energy of spectator neutrons with an energy resolution of $\sigma(E)/E = 85\%/\sqrt{E} + 9.1\%$. The SMDs [34] are scintillator strip hodoscopes located between the first and second ZDC modules, a location corresponding approximately to the maximum of the hadronic shower. The horizontal coordinate is sampled by seven scintillator strips of 15 mm width, while the vertical coordinate is sampled by eight strips of 20 mm width. The active area of each SMD is 105 mm \times 110 mm (horizontal \times vertical dimension). Scintillation light is delivered to a multichannel Hamamatsu PMT R5900-M16 by wavelength-shifting fibers [34]. A typical position resolution for SMD is ~ 0.1 – 0.3 cm.

B. Tracking and particle identification detectors

The charged-particle momentum is reconstructed by using the tracking system. This system comprises the DC, located outside an axially symmetric magnetic field at a radial distance between 2.0 and 2.4 m, followed by PC1-3. The pattern recognition in the DC is based on a combinatorial Hough transform [35] in the track bend plane. A track model based on a field-integral look-up table determines the charged-particle momentum, the path length to the time-of-flight detector, and a projection of the track to the outer detectors.

The tracks are matched to hits registered in the PC3 and the EMCal, thus reducing the contribution of tracks originating from decays and γ conversions.

The primary particle identification detectors used in this analysis are the time-of-flight detectors. The different detectors in the east and west arms use different technologies (scintillators and MRPCs, respectively) and have different time resolutions [36,37]. The total timing resolutions (including the start time measurement from the BBC) are 130 ps and 95 ps for east and west, respectively. Pion, kaon, and (anti)proton tracks are

TABLE I. Number of participants and the participant eccentricity ($\varepsilon_2, \varepsilon_3$) from Monte Carlo Glauber calculations for Au + Au, Cu + Cu, and Cu + Au collisions at 200 GeV

Centrality bin	Au + Au 200 GeV			Cu + Cu 200 GeV		Cu + Au 200 GeV		
	N_{part}	ε_2	ε_3	N_{part}	ε_2	N_{part}	ε_2	ε_3
0%–10%	325.2 ± 3.3	0.103 ± 0.003	0.087 ± 0.002	98.2 ± 2.4	0.163 ± 0.003	177.2 ± 5.2	0.138 ± 0.011	0.130 ± 0.004
10%–20%	234.6 ± 4.7	0.200 ± 0.005	0.122 ± 0.004	73.6 ± 2.5	0.241 ± 0.007	132.4 ± 3.7	0.204 ± 0.008	0.161 ± 0.005
20%–30%	166.6 ± 5.4	0.284 ± 0.006	0.156 ± 0.005	53.0 ± 1.9	0.317 ± 0.006	95.1 ± 3.2	0.280 ± 0.008	0.208 ± 0.007
30%–40%	114.2 ± 4.4	0.356 ± 0.006	0.198 ± 0.008	37.3 ± 1.6	0.401 ± 0.008	65.7 ± 3.4	0.357 ± 0.010	0.266 ± 0.010
40%–50%	74.4 ± 3.8	0.422 ± 0.006	0.253 ± 0.011	25.4 ± 1.3	0.484 ± 0.008	43.3 ± 3.0	0.436 ± 0.013	0.332 ± 0.013
50%–60%	45.5 ± 3.3	0.491 ± 0.005	0.325 ± 0.018	16.7 ± 0.9	0.579 ± 0.008	26.8 ± 2.6	0.523 ± 0.019	0.412 ± 0.019

identified with over 97% purity for $p_T < 2$ GeV/ c [36,38] in both systems. For p_T between 2 to 3 GeV/ c , the purity of pions and protons is about 95% and that of kaons is around 90%.

C. Anisotropic flow measurement technique

The present measurements use the event-plane method [39] to quantify the azimuthal anisotropies of the particles produced in Cu + Au collisions. The v_1 , v_2 , and v_3 Fourier coefficients are determined as a function of centrality and p_T for inclusive charged particles and identified hadrons π^\pm , K^\pm , p , and \bar{p} (with charge signs combined).

In the event-plane method, a measured event-plane direction Ψ_n^{obs} is determined for every event and for each order n . The harmonic coefficients $v_n\{\Psi_n\} = \langle \cos n(\phi - \Psi_n^{\text{obs}}) \rangle / \text{Res}\{\Psi_n\}$ are then measured with respect to the event plane for each harmonic, where ϕ is the azimuthal angle of the hadron and $\text{Res}\{\Psi_n\}$ is the event-plane resolution.

The collision geometry of a Cu + Au collision is shown in Fig. 2(a) projected onto the reaction plane, and in Fig. 2(b) projected onto the plane perpendicular to the beam axis. Figure 2(a) shows direction of the projectile (Cu) and target (Au) spectators, which are bent away from the participant zone. There is an alternative picture, in which the spectators are attracted towards the center of the system, as discussed in Ref. [40]. In this paper, we assume the former picture for the determination of the direction of the event-plane angle from the spectators.

As shown in Fig. 2(a), the Cu spectators fly along the the positive-rapidity direction (north) and the Au spectators go towards the negative-rapidity direction (south). The central position of the Au spectators is measured by the south SMD (SMDS) to determine the spectator plane Ψ_1^{SMDS} . The v_1 of charged and identified hadrons is measured with respect to Ψ_1^{SMDS} , as indicated in Eq. (1). Measurement with respect to the spectator plane is preferred over the first-order event-plane determined by the distribution of the produced particles, because the distribution of the spectators is less distorted by momentum-conservation effects:

$$v_1 = -\frac{\langle \cos(\phi_{\text{track}} - \Psi_1^{\text{SMDS}}) \rangle}{\text{Res}(\Psi_1^{\text{SMDS}})} \quad (1)$$

$$\text{Res}(\Psi_1^{\text{SMDS}}) = \langle \cos(\Psi_1^{\text{SMDS}} - \Psi_1) \rangle$$

$$= \sqrt{\frac{\langle \cos(\Psi_1^{\text{SMDS}} - \Psi_1^{\text{SMDN}}) \rangle \langle \cos(\Psi_1^{\text{SMDS}} - \Psi_1^{\text{BBCSN}}) \rangle}{\langle \cos(\Psi_1^{\text{SMDN}} - \Psi_1^{\text{BBCSN}}) \rangle}}. \quad (2)$$

TABLE II. Systematic uncertainties in the v_1 measurements.

v_1	Uncertainty sources	10%–20%	40%–50%	Type
v_1	Event plane	20%	12%	C
	Background (absolute value)	5×10^{-4}	5×10^{-4}	A
	Acceptance (absolute value)	3×10^{-3}	2×10^{-3}	C

TABLE III. Systematic uncertainties given in percent on the v_2 and v_3 measurements.

v_n ($n = 2, 3$)	Uncertainty sources	0%–10%	20%–30%	Type
v_2	Event plane	3%	4%	B
	Background	2%	2%	A
	Acceptance	2%	3%	C
v_3	Event plane	3%	7%	B
	Background	2%	2%	A
	Acceptance	8%	10%	C

There is a negative sign in Eq. (1) to keep the convention in which the direction of projectile (Cu) spectators is positive. In Eq. (2) the resolution of Ψ_1^{SMDS} is calculated in 10% centrality intervals with the three-subevent method [39,41] by combining the other Cu spectator plane from the north SMD (SMDN) and the first-order participant event-plane measured by the combined south and north BBCs (BBCSN). However, this method for determining the resolution assumes a nonfluctuating nuclear-matter distribution. Event-by-event fluctuations in the initial energy density of the collision will cause the v_1 signal to be different with respect to Ψ_1^{SMDS} and Ψ_1^{SMDN} due to the rapidity-symmetric component in the direct flow [18]. To cover this uncertainty, the resolution of Ψ_1^{SMDS} is also calculated by using the participant plane from either BBCS or BBCN and the differences are assigned as a systematic uncertainty.

The second-order (Ψ_2) and third-order (Ψ_3) event planes are measured by the combination of BBCS and BBCN. To determine the second- and third-order event-plane resolution from the BBC, we first measure the second- and third-order event planes with the BBCS (Au-going side), BBCN (Cu-going side) and central arm tracks (CNTs). The central-arm tracks are restricted to low p_T ($0.2 < p_T < 2.0$ GeV/ c) to minimize the contribution from jet fragments. The second- and third-order event-plane resolution of BBCS, BBCN, and CNT are calculated by using three subevent methods with a combination of BBCS-BBCN-CNT. Then the second- and third-order event-plane resolutions of the BBC (including both BBCS and BBCN) are calculated with two subevent methods with a combination of BBC-CNT.

The event-plane resolutions for different subsystems are shown in Fig. 3 as a function of centrality. Figure 3(a) shows the resolution of the first-order event plane as measured by the SMDS using three different methods. The first method uses a three-subevent combination SMDS-BBCSN-SMDN, shown with circles, the second method shown with open squares uses a three-subevent combination SMDS-BBCS-SMDN, and the

TABLE IV. Systematic uncertainties in the measured v_1 for identified particles.

Species	$p_T \leq 2$ GeV/ c	$p_T \geq 2$ GeV/ c	Type
Pion (absolute value)	1×10^{-3}	2×10^{-3}	A
Kaon (absolute value)	1×10^{-3}	3×10^{-3}	A
Proton (absolute value)	1×10^{-3}	3×10^{-3}	A

TABLE V. Systematic uncertainties in percent on the measured v_2 and v_3 for identified particles.

Species	$p_T \leq 2$ GeV/c	$p_T \geq 2$ GeV/c	Type
Pion	3%	5%	A
Kaon	3%	10%	A
Proton	3%	5%	A

third method shown with open triangles uses the combination SMDS-BBCN-SMDN.

The resolution of the second- and third-order event planes for BBC, BBCS, BBCN, and CNT are shown in Figs. 3(a) and 3(c), respectively.

D. Number of participants and eccentricity

A Monte Carlo Glauber simulation was used to estimate the average number of participating nucleons N_{part} and the eccentricity,

$$\varepsilon_n = \frac{\sqrt{\langle r^2 \cos(n\phi) \rangle^2 + \langle r^2 \sin(n\phi) \rangle^2}}{\langle r^2 \rangle}. \quad (3)$$

This simulation employed a Glauber model with a Woods–Saxon density profile and includes modeling of the BBC response [11,42]. The eccentricity defined in Eq. (3) is also known as the participant eccentricity $\varepsilon_{\text{part}}$ and includes the effect of fluctuations from the initial participant geometry. Table I summarizes N_{part} and ε_n .

E. Data set

The measurements presented here use data from Cu + Au collisions at $\sqrt{s_{NN}} = 200$ GeV collected by the PHENIX experiment at RHIC in 2012. Minimum-bias events triggered by the BBC recorded within ± 30 cm from the nominal interaction point along the z axis were used. The events were examined to ensure that stable performance is seen in the detectors used in the analysis; namely, DC, PC3, TOF, BBC, and SMD. A total of 3.6×10^9 events were analyzed.

F. Systematic uncertainties

Tables II–V summarize the systematic uncertainties for the measurements of v_1 , v_2 , and v_3 for inclusive and identified charged hadrons, which are categorized by the types:

- (A) point-to-point uncertainties uncorrelated between p_T bins;
- (B) p_T correlated, all points move in a correlated manner, but not by the same factor;
- (C) an overall normalization error in which all points move by the same multiplicative factor independent of p_T .

Contributions to the uncertainties are from the following sources:

- (1) event-plane resolution correction,
- (2) event plane as measured using different detectors,
- (3) v_n from background tracks,
- (4) acceptance dependencies,
- (5) PID purity.

The uncertainties from measurements of the event planes using different detectors are found to depend only weakly on p_T . For the measurement of v_1 , the uncertainties are obtained by comparing v_1 as measured with SMDS with alternately BBCN or BBCS used for resolution. For v_2 and v_3 , the uncertainties are obtained by comparing v_2 and v_3 as measured by the BBCN and BBCS. For the v_1 measurement, for the 10%–20% centrality class we find a 20% systematic uncertainty independent of p_T . For the 40%–50% centrality class, we find a 12% systematic uncertainty. For v_2 , the systematic uncertainty is less than 3% for the 0%–10% centrality range and increases to 4% for the centrality range 50%–60%. For v_3 , a 3% systematic uncertainty is found for 0%–10% centrality, increasing to 7% for the 20%–30% centrality range.

Background tracks that are not removed by the tracking selections as described in Sec. II may influence the measured v_n . They can arise from particle decays, γ conversions, or false track reconstruction. We estimate the tracking background contribution by varying the width of the track-matching window in PC3 and comparing the results with and without the EMCal matching cut. We find that the absolute uncertainty for v_1 is less than 5×10^{-4} . For v_2 and v_3 , the change is less than 2%.

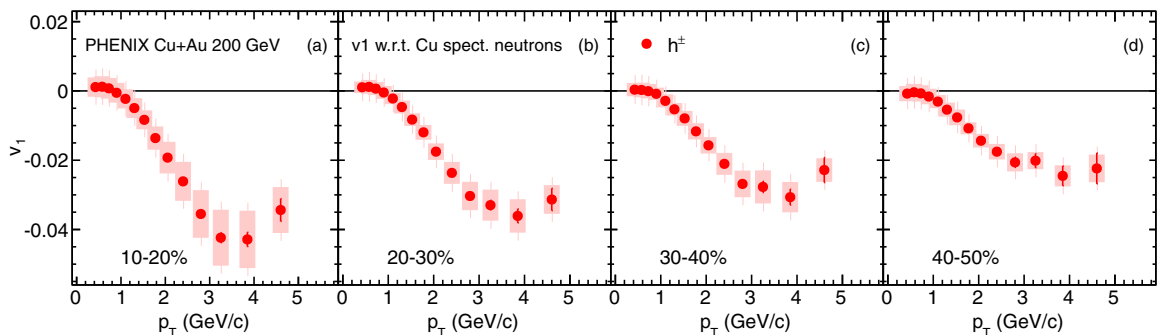


FIG. 4. $v_1(p_T)$ for charged hadrons measured with respect to the Cu spectator neutrons at midrapidity in Cu + Au collisions at $\sqrt{s_{NN}} = 200$ GeV. Error bars show the statistical uncertainties, and shaded boxes indicate the systematic uncertainties.

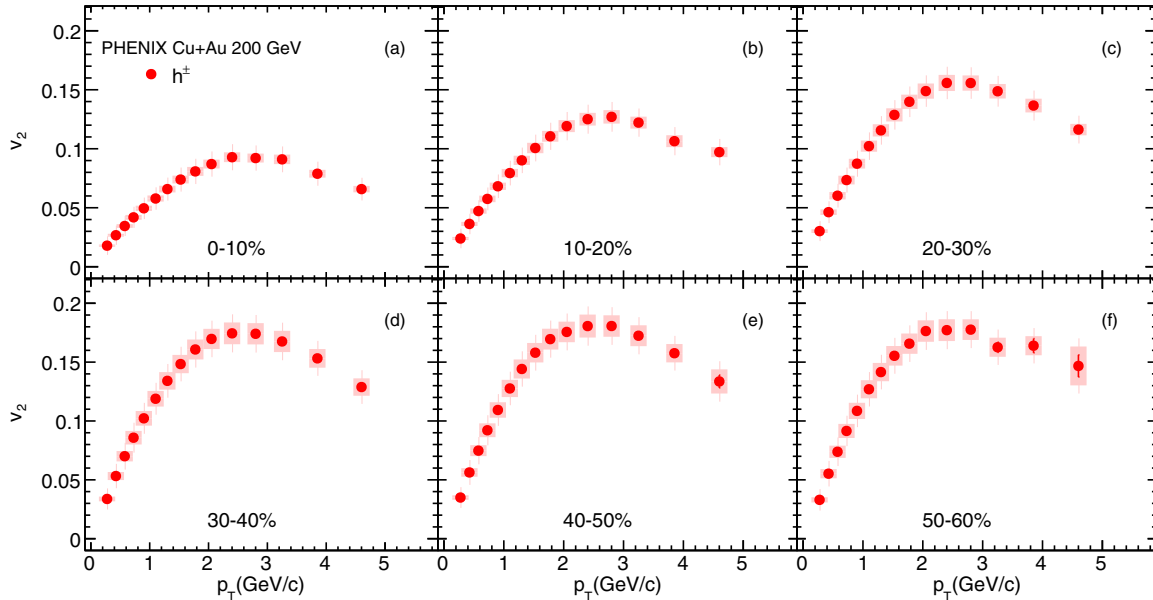


FIG. 5. $v_2(p_T)$ for charged hadrons measured at midrapidity in Cu + Au collisions at $\sqrt{s_{NN}} = 200$ GeV. Uncertainties are as in Fig. 4.

Systematic uncertainties of acceptance were evaluated by using different subsets of the detector such as DC and TOF in the east and west arms. Differences in v_n measured by using different arms may be caused by different detector alignment and performance. Maximum differences of order 3% and 10% were found for v_2 and v_3 , respectively. These uncertainties have centrality dependence and minimal p_T dependence. For v_1 , a maximum absolute uncertainty of 3×10^{-3} is found. These uncertainties are detailed further in Tables II and III.

An additional systematic uncertainty in v_n resulting from hadron misidentification is based on the PID purity estimates from the TOF detectors as discussed in Sec. II. Pion, kaon, and proton species purity is greater than 90% and the differences between their corresponding v_n is less than a factor of two. For v_2 and v_3 , an additional uncertainty of 3% (type A) attributable to contamination from other species is found for particles with $p_T < 2$ GeV/c, 5% for higher- p_T pions and protons, and 10% for higher- p_T kaons. In the measurements of v_1 , a common absolute uncertainty of 1×10^{-3} is found for the three particle species for $p_T < 2$ GeV/c, and at higher p_T the uncertainties are 2×10^{-3} for pions and 3×10^{-3} for kaons and protons,

respectively. The uncertainties due to particle identification are to be added in quadrature to the values listed in Tables II and III.

III. RESULTS AND DISCUSSION

A. Harmonic-flow results from Cu + Au collisions

Figures 4–6 show the v_1 , v_2 , and v_3 results for charge-combined hadrons measured as a function of p_T in Cu + Au collisions at $\sqrt{s_{NN}} = 200$ GeV. Different centrality intervals are studied. The filled circles show the $v_n(p_T)$ data, and the systematic uncertainties are shown with the shaded boxes.

The $v_1(p_T)$ measurements shown in Fig. 4 are performed with respect to the event plane determined by spectator neutrons from the Au nucleus. To align with previous conventions, we flip the sign so that it is effectively with respect to the spectator neutrons from the Cu nucleus, as noted in Sec. IIC. In all centrality intervals, high- p_T particles at midrapidity move in the direction opposite of the Cu nucleus spectator neutrons, as indicated by the negative v_1 values. Low- p_T particles might then be expected to move in the opposite direction by conservation of momentum, and there is a hint of

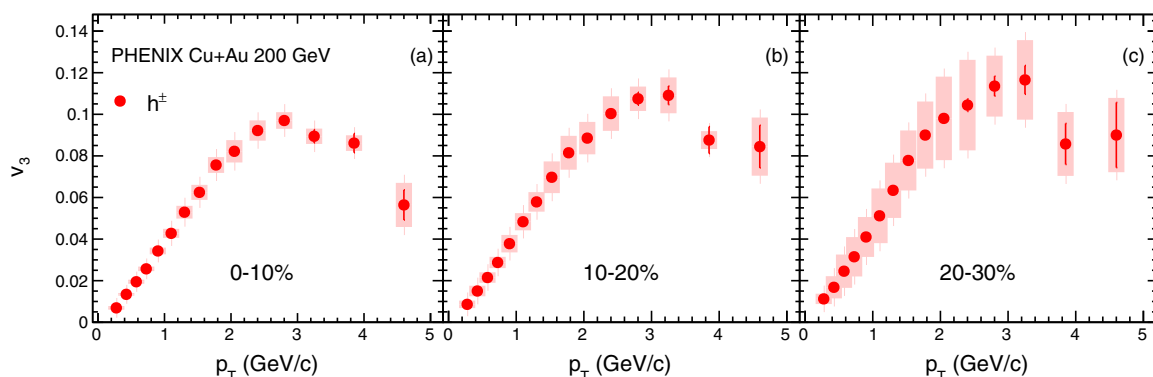


FIG. 6. $v_3(p_T)$ for charged hadrons measured at midrapidity in Cu + Au collisions at $\sqrt{s_{NN}} = 200$ GeV. Uncertainties are as in Fig. 4.

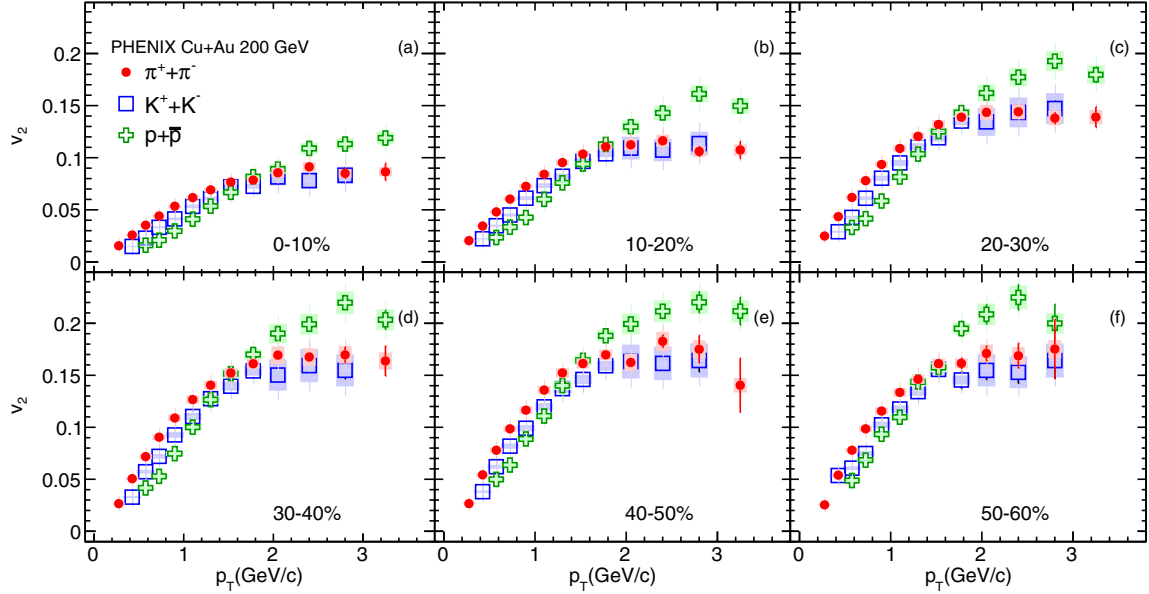


FIG. 7. The second-order Fourier coefficients $v_2(p_T)$ for charge-combined identified hadrons π^\pm , K^\pm , p , and \bar{p} measured at midrapidity in Cu + Au collisions at $\sqrt{s_{NN}} = 200$ GeV for the centrality classes marked in each panel. The symbols represent the measured $v_2(p_T)$ values, the error bars show the statistical uncertainties, and the shaded boxes indicate the systematic uncertainties from PID. The full systematic uncertainties, that are mostly common to all particle species, are shown in Table III.

this effect though not beyond current systematic uncertainties. The v_1 component is consistent with zero for $p_T < 1$ GeV/c and its absolute value increases at higher p_T . The maximum of the absolute value decreases from central to peripheral collisions. This is contrary to the centrality dependence of v_2 where the values increase from the most-central 0%–10% collisions, up to the 30%–40% centrality class. This trend in v_2 is expected from the initial geometry, because the ellipticity of the participant zone ε_2 (see Table I) increases in the peripheral collisions. The $v_2(p_T)$ values in the 30%–40%, 40%–50%, and 50%–60% Cu + Au centrality classes, shown in Fig. 5 are consistent with each other, showing very little, if any, centrality dependence. The v_2 and v_3 values are positive, as previously observed in symmetric-collision systems. For all three harmonics, the magnitude of the signal increases with p_T up to about $p_T = 3$ GeV/c, and then tends to decrease. This may indicate a change in the dominant production mechanism, e.g., an increasing contribution from jet fragments, or it may be due to the fact that higher- p_T particles escape the fireball with fewer interactions.

The v_3 component (Fig. 6) has weak centrality dependence; a behavior which is similar in symmetric $A + A$ collisions [21,22], where the triangular flow at midrapidity is completely driven by the event-by-event fluctuations of the interaction zone. These fluctuations are also present in the asymmetric Cu + Au collisions and are expected to play a similar role. In Sec. III C we compare the flow results obtained in different collisions systems and explore their scaling behavior.

B. Identified particle flow results

Figures 7 and 8 show the particle-species dependence of v_2 and v_3 in Cu + Au collisions. Results are presented for charge-

combined π^\pm , K^\pm , p , and \bar{p} . The measured $v_n(p_T)$ values are shown with points, and the shaded boxes represent the species-dependent type-A systematic uncertainties. The type-B and -C systematic uncertainties shown in Table III are largely common for all particle species. For the odd harmonics, to improve the statistical significance of the results the measurements for identified particles are performed in a single centrality interval; namely, 0%–30% for $v_3(p_T)$ and 10%–50% for $v_1(p_T)$.

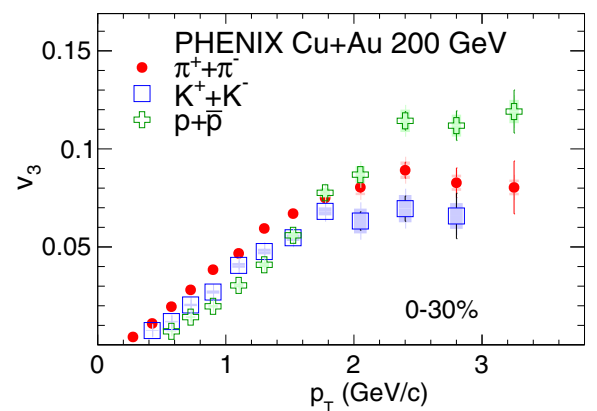


FIG. 8. The third-order Fourier coefficients $v_3(p_T)$ for charge-combined identified hadrons π^\pm , K^\pm , p , and \bar{p} measured at midrapidity in Cu + Au collisions at $\sqrt{s_{NN}} = 200$ GeV for 0%–30% centrality. The symbols represent the measured $v_3(p_T)$ values, the error bars show the statistical uncertainties, and the shaded boxes indicate the systematic uncertainties from PID. The full systematic uncertainties, which are mostly common to all particle species, are shown in Table III.

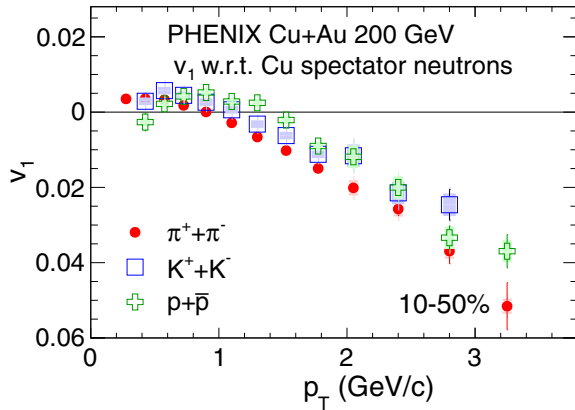


FIG. 9. The first-order Fourier coefficients $v_1(p_T)$ for charge-combined identified hadrons π^\pm , K^\pm , p , and \bar{p} measured at midrapidity in Cu + Au collisions at $\sqrt{s_{NN}} = 200$ GeV for 10%–50% centrality. The symbols represent the measured $v_1(p_T)$ values with respect to the Cu spectator neutrons, the error bars show the statistical uncertainties, and the shaded boxes indicate the systematic uncertainties from PID. The full systematic uncertainties, which are mostly common to all particle species, are shown in Table II.

There are two trends common to both the $n = 2, 3$ results shown in Figs. 7 and 8: First, in the low- p_T region the anisotropy appears largest for the lightest hadron and smallest for the heaviest hadron. A similar mass ordering is also predicted by hydrodynamics, in which all particles are moving in a common velocity field. Second, for $p_T \geq 2$ GeV/c this mass dependence is reversed, such that the anisotropy is larger for the baryons than it is for mesons at the same p_T . These

patterns have been observed previously in v_n measurements for identified particles in Au + Au collisions at RHIC. The $v_1(p_T)$ values, presented in Fig. 9, also show mass ordering, although these measurements have larger overall systematic and statistical uncertainties than $v_2(p_T)$ and $v_3(p_T)$. As in the case of $v_1(p_T)$ for charged particles described in Sec. III (Fig. 4), we note that, although the values of $v_1(p_T)$ for each species appear to be positive at low p_T , if the full systematic uncertainty of types B and C is taken into account, a definitive conclusion cannot be drawn about the overall sign of the bulk directed flow. The mass dependence in the collective flow at low p_T is a generic feature of hydrodynamical models. The dependence on valence quark number in the intermediate- p_T region has been associated with the development of flow in the partonic phase of the fireball evolution and subsequent hadronization by parton coalescence [43].

C. System-size dependence

It is interesting to compare the charged-hadron $v_n(p_T)$ results for different collision systems measured in the same experiment at the same center-of-mass energy. PHENIX has previously studied anisotropic flow harmonics in symmetric Au + Au and Cu + Cu collisions at $\sqrt{s_{NN}} = 200$ GeV [12,22]. By varying the system size and the centrality selection, one can study the effects of the initial geometry on the observed flow coefficients. We first compare the results obtained in different collision systems for the same centrality selections, and then explore possible scaling behavior.

In Fig. 10, the $v_2(p_T)$ coefficients are compared for six different centrality selections. We observe that, in each centrality class at a given p_T , the values measured in Cu + Au

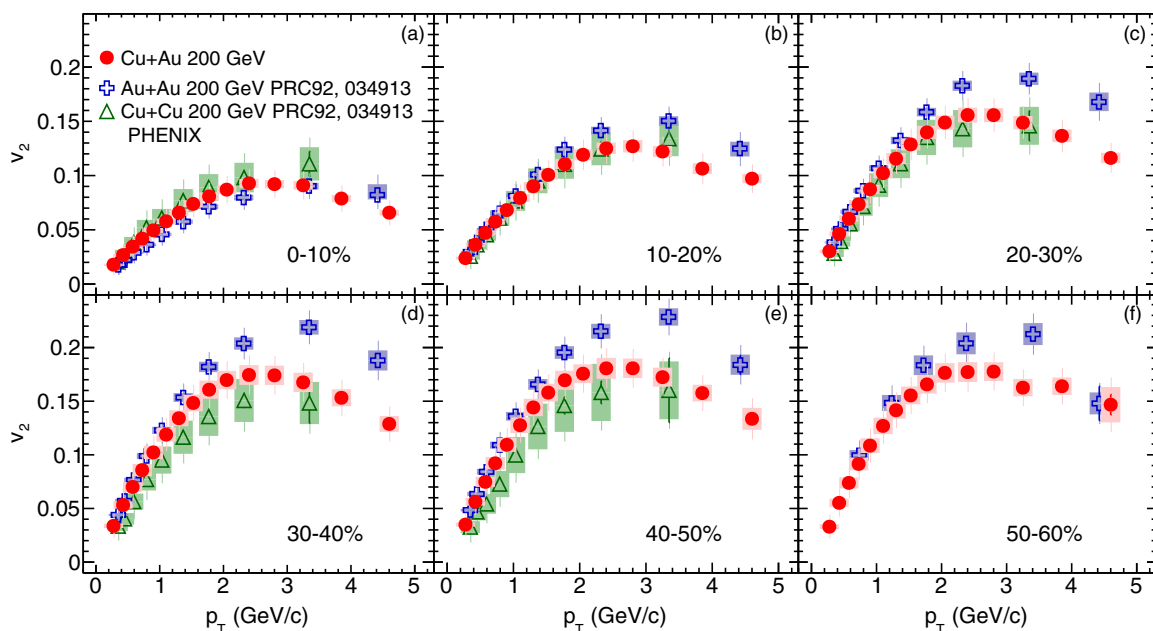


FIG. 10. The second-order Fourier coefficients $v_2(p_T)$ for charged hadrons measured at midrapidity in Cu + Au, Au + Au [12], and Cu + Cu [12] collisions at $\sqrt{s_{NN}} = 200$ GeV. In each panel, the $v_2(p_T)$ coefficients are compared for the same centrality class, as marked in the figure. The symbols represent the measured $v_2(p_T)$ values, the error bars show the statistical uncertainties, and the shaded boxes indicate the systematic uncertainties.

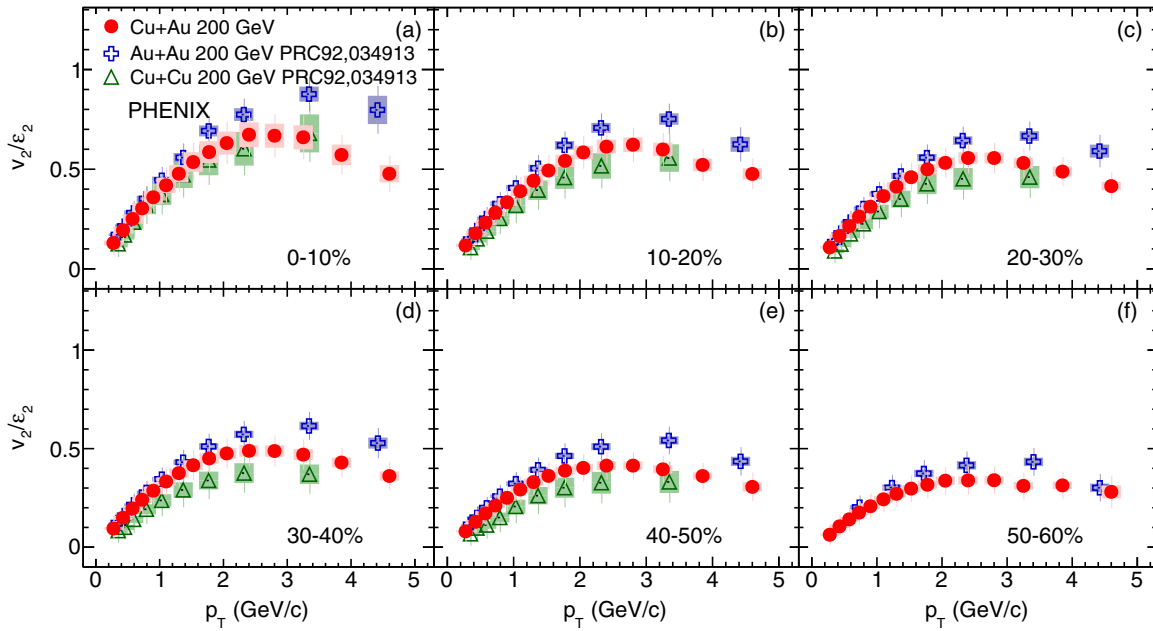


FIG. 11. Scaled second-order Fourier coefficients $v_2(p_T)/\epsilon_2$ for charged hadrons measured at midrapidity in Cu + Au, Au + Au [12], and Cu + Cu [12] collisions at $\sqrt{s_{NN}} = 200$ GeV. In each panel, the $v_2(p_T)$ values measured in the centrality classes marked in the figure are scaled by the average second-order participant eccentricity ϵ_2 in the initial state of the collisions as determined by a Monte Carlo Glauber calculation described in the text. The symbols represent the scaled $v_2(p_T)/\epsilon_2$ values, the error bars show the statistical uncertainties, and the shaded boxes indicate the systematic uncertainties.

collisions are always between those measured in Cu + Au and Au + Au collisions. In all centrality classes chosen, the Cu + Cu system has larger elliptic eccentricity than both Cu + Au and Au + Au collisions. However, except in the

most-central 0%–10% collisions, the measured $v_2(p_T)$ values are not ordered according to the magnitude of ϵ_2 in the different systems listed in Table I. To further investigate this, in Fig. 11 we scale the $v_2(p_T)$ values in each collision system with their

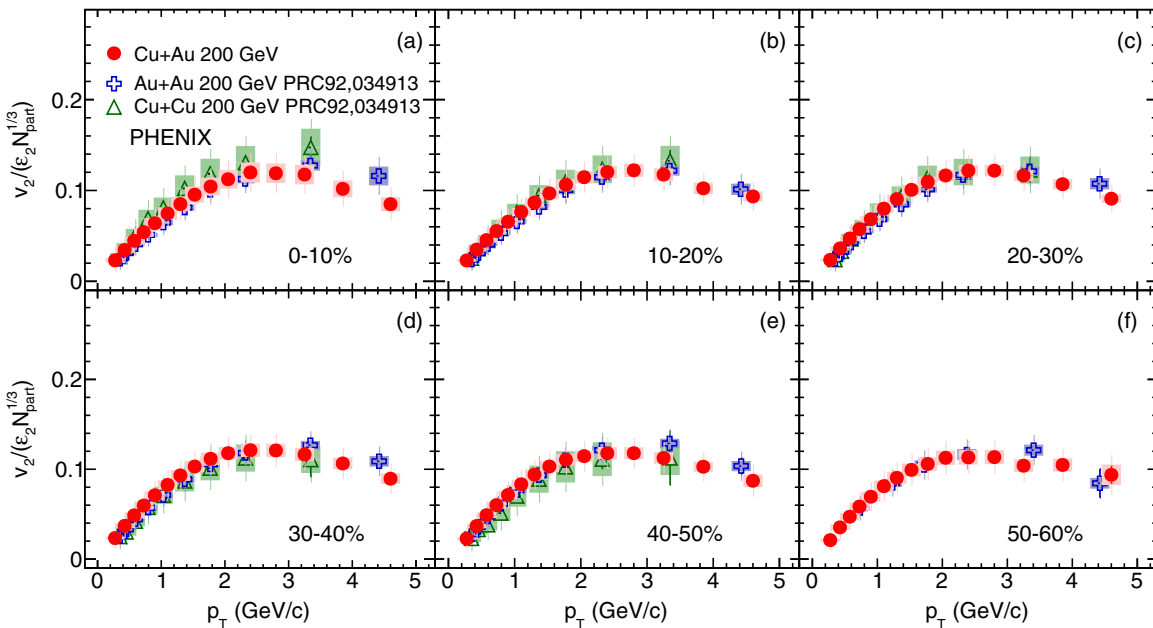


FIG. 12. Scaled second-order Fourier coefficients $v_2(p_T)/(\epsilon_2 N_{\text{part}}^{1/3})$ for charged hadrons measured at midrapidity in Cu + Au, Au + Au [12], and Cu + Cu [12] collisions at $\sqrt{s_{NN}} = 200$ GeV. In each panel, the $v_2(p_T)$ values measured in the centrality classes marked in the figure are scaled by the average second-order participant eccentricity ϵ_2 in the initial state of the collisions as determined by a Monte Carlo Glauber calculation described in the text, and the corresponding number of nucleon participants $N_{\text{part}}^{1/3}$. The symbols represent the scaled $v_2(p_T)/(\epsilon_2 N_{\text{part}}^{1/3})$ values, the error bars show the statistical uncertainties, and the shaded boxes indicate the systematic uncertainties.

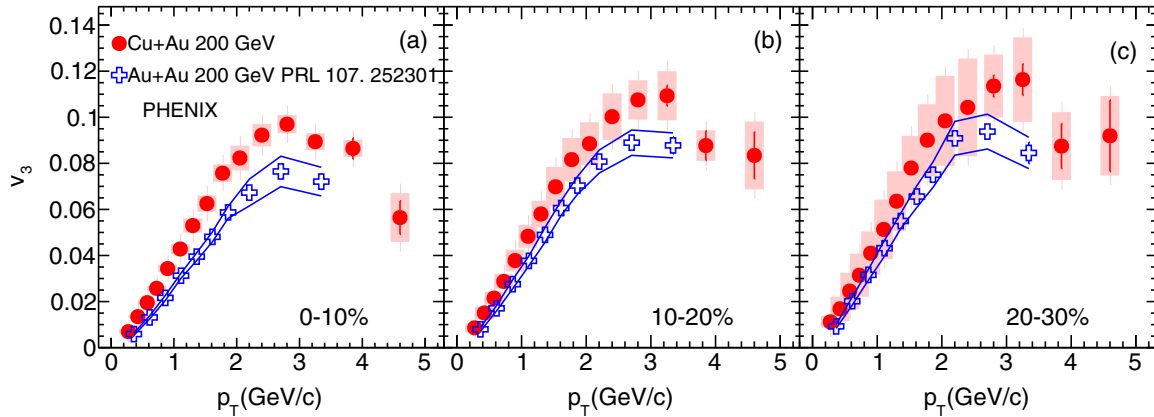


FIG. 13. The third-order Fourier coefficients $v_3(p_T)$ for charged hadrons measured at midrapidity in Cu + Au and Au + Au [22] collisions at $\sqrt{s_{NN}} = 200$ GeV. In each panel, the $v_3(p_T)$ coefficients are compared for the same centrality class, as marked in the figure. The symbols represent the measured $v_3(p_T)$ values, the error bars show the statistical uncertainties, and the shaded boxes indicate the systematic uncertainties.

respective participant eccentricity ε_2 . The resulting $v_2(p_T)/\varepsilon_2$ are ordered by system size, but this scaling does not lead to a universal behavior.

In Ref. [12], PHENIX compared measurements in Cu + Cu and Au + Au collisions for different center-of-mass energies and centrality selections and found that the v_2 values obey common empirical scaling with $\varepsilon_2 N_{\text{part}}^{1/3}$. The motivation for introducing the $N_{\text{part}}^{1/3}$ factor is that, under the assumption that N_{part} is proportional to the volume of the fireball, $N_{\text{part}}^{1/3}$ is a quantity proportional to a length scale and therefore may account for the system-size dependence of the v_2 values. In Fig. 12 we add to this comparison the results from the asymmetric Cu + Au collisions. This scaling brings the $v_2(p_T)$ results from the three collisions systems together across all centrality classes in this study.

In Fig. 13 the $v_3(p_T)$ values are compared in Cu + Au and Au + Au collisions for events of the same centrality.

Unlike in the $v_2(p_T)$ measurements, here the values of $v_3(p_T)$ are ordered according to the initial triangularities ε_3 listed in Table I, with the Cu + Au results being larger than the Au + Au results. In particular, in the most-central 0%–10% collisions ε_3 in Cu + Au is about 50% larger than in Au + Au collisions, and a similar difference is observed in the $v_3(p_T)$ values. In Fig. 14 the $v_3(p_T)$ values are scaled by the initial ε_3 eccentricity. A good agreement between the different systems is observed at low p_T (≤ 2 GeV/c), which indicates that the participant eccentricities obtained in the Glauber model provide an adequate description of the fluctuating initial geometry. Additionally, we perform scaling with $\varepsilon_3 N_{\text{part}}^{1/3}$, as was done for the $v_2(p_T)$ measurements. The results of this scaling are shown in Fig. 15. In this case, the measurement in Cu + Au and Au + Au collisions are in better agreement at high p_T ; however, at low p_T the $v_3(p_T)/\varepsilon_3 N_{\text{part}}^{1/3}$ values are systematically higher for the Cu + Au system.

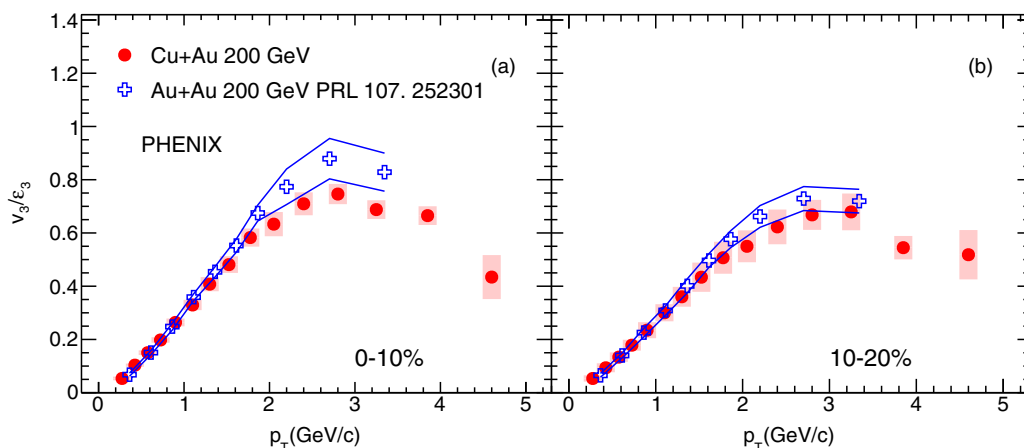


FIG. 14. Scaled third-order Fourier coefficients $v_3(p_T)/\varepsilon_3$ for charged hadrons measured at midrapidity in Cu + Au and Au + Au [22] collisions at $\sqrt{s_{NN}} = 200$ GeV. In each panel, the $v_3(p_T)$ values measured in the centrality classes marked in the figure are scaled by the average third-order participant eccentricity ε_3 in the initial state of the collisions as determined by a Monte Carlo Glauber calculation described in the text. The symbols represent the scaled $v_3(p_T)/\varepsilon_3$ values, and the error bars show the statistical uncertainties. The shaded boxes indicate the systematic uncertainties in the Cu + Au measurements, and the lines around the points marked with a cross show the systematic uncertainties in the Au + Au measurements.

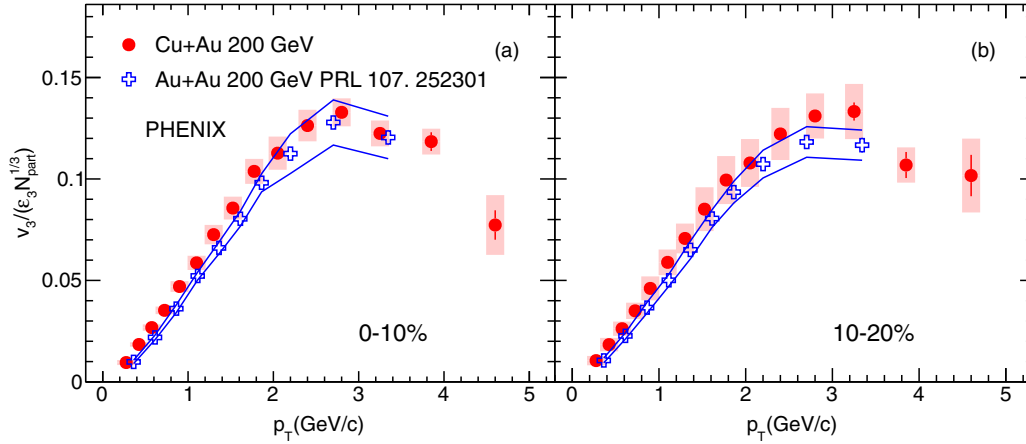


FIG. 15. Scaled third-order Fourier coefficients $v_3(p_T)/(\epsilon_3 N_{\text{part}}^{1/3})$ for charged hadrons measured at midrapidity in Cu + Au and Au + Au [22] collisions at $\sqrt{s_{NN}} = 200$ GeV. In each panel, the $v_3(p_T)$ values measured in the centrality classes marked in the figure are scaled by the average third-order participant eccentricity ϵ_3 in the initial state of the collisions as determined by a Monte Carlo Glauber calculation described in the text and the corresponding number of nucleon participants $N_{\text{part}}^{1/3}$. The symbols represent the scaled $v_3(p_T)/(\epsilon_3 N_{\text{part}}^{1/3})$ values, and the error bars show the statistical uncertainties. The shaded boxes indicate the systematic uncertainties in the Cu + Au measurements, and the lines around the points marked with a cross show the systematic uncertainties in the Au + Au measurements.

D. Theory comparisons

1. Hydrodynamic calculations

Predictions from 3D + 1 viscous hydrodynamic calculations are available [44]. At low p_T (< 1.0 GeV/ c), directed flow is predicted to be in the hemisphere of the Cu side, while for high p_T (> 1.5 GeV/ c), directed flow is predicted to be in the hemisphere on the Au side. Furthermore, the bulk directed flow component from integration over p_T is predicted to be in the Cu-nucleus hemisphere. Due to the large systematic uncertainties and small value of v_1 at small p_T , we cannot reliably determine the sign of the v_1 component at low p_T , or the sign of the bulk directed flow. At high p_T , the measurement is in agreement with the directed flow being in the Au hemisphere, under the assumption that the spectator neutrons

are deflected outward from the interaction region and aligned with the impact parameter vector. Reference [44] shows v_1 with respect to the reaction plane (i.e., the impact parameter vector) for 20%–30% central Cu + Au collisions including particles within $|\eta| < 1.0$, and thus we cannot compare directly with our narrower rapidity selection. It is notable however, that the hydrodynamic results at $p_T = 2$ GeV/ c reach $v_1 \approx 5\%$, while the experimental data within $|\eta| < 0.35$ are less than 2%.

The predictions for elliptic and triangular flow as a function of p_T are compared with the data in Figs. 16 and 17. Calculations with two different values of the specific viscosity $\eta/s = 0.08$ and $\eta/s = 0.16$ are shown. Our measurements in the 20%–30% centrality range are consistent with each of these values; for the most-central 0%–5% events, a value of $\eta/s = 0.08$ is closer to the data.

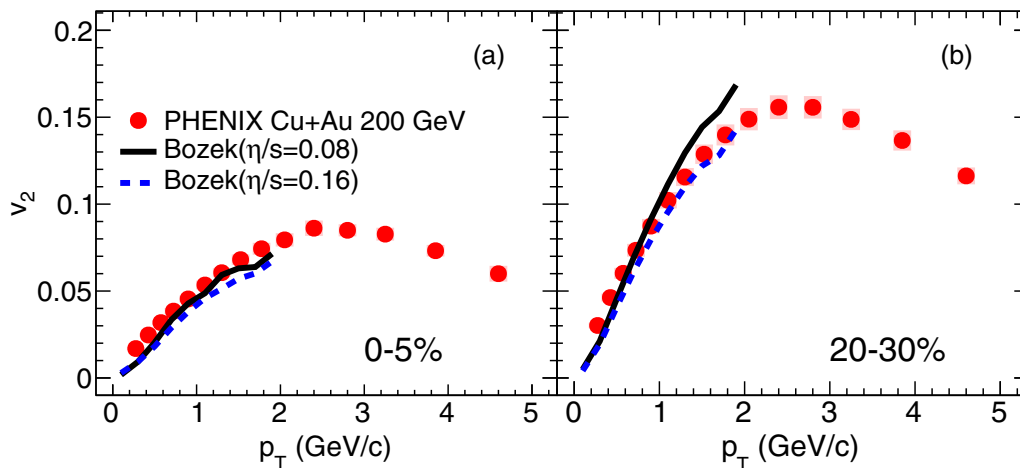


FIG. 16. The second-order Fourier coefficients $v_2(p_T)$ for charged hadrons measured at midrapidity in Cu + Au collisions at $\sqrt{s_{NN}} = 200$ GeV in comparison with hydrodynamics calculations for the centrality classes marked in each panel. The symbols represent the measured $v_2(p_T)$ values, the error bars show the statistical uncertainties, and the shaded boxes indicate the systematic uncertainties. The theoretical calculations, shown with the solid and dashed lines, are performed with two different values of the specific viscosity η/s marked in the figure.

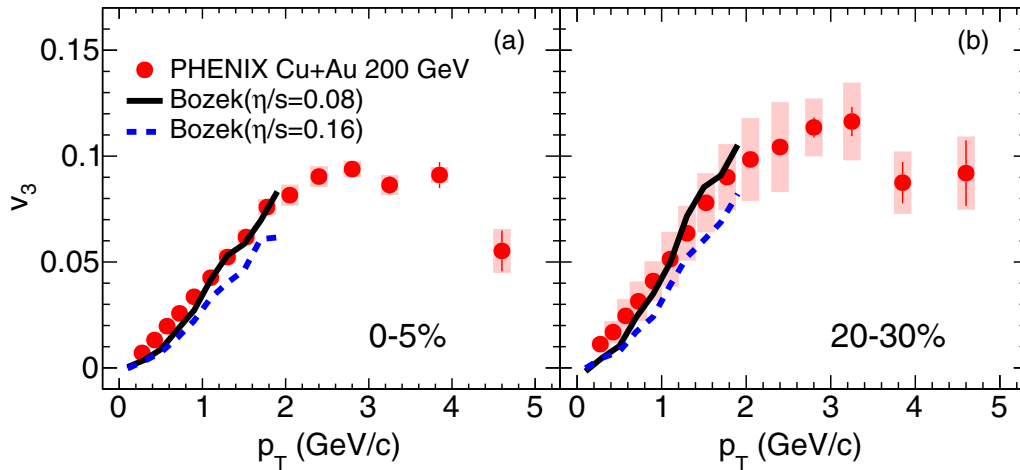


FIG. 17. The third-order Fourier coefficients $v_3(p_T)$ for charged hadrons measured at midrapidity in Cu + Au collisions at $\sqrt{s_{NN}} = 200$ GeV in comparison with hydrodynamics calculations for the centrality classes marked in each panel. The symbols represent the measured $v_3(p_T)$ values, the error bars show the statistical uncertainties, and the shaded boxes indicate the systematic uncertainties. The theoretical calculations, shown with the solid and dashed lines, are performed with two different values of the specific viscosity η/s marked in the figure.

2. A Multiphase Transport Model

The multiphase transport model (AMPT) generator [45,46] has been established as a useful tool in the study of flow observables in heavy-ion collisions [47]. Therefore, it is of interest to compare the measured v_1 , v_2 , and v_3 as a function of p_T with the corresponding quantities calculated by using the AMPT model. To this end, we used AMPT v2.21 with string melting turned on to generate approximately two million minimum bias Cu + Au events at $\sqrt{s_{NN}} = 200$ GeV, setting the partonic cross section alternately to $\sigma_{\text{part}} = 1.5$ and 3.0 mb. In the default version of the model, initial conditions are

generated by using Monte Carlo Glauber with a *gray-disk* approach to nucleon-nucleon interactions. However, in this study we utilize a modified *black-disk* Glauber model with a fixed nucleon-nucleon inelastic cross section of 42 mb, as used in Ref. [47].

Following the method of Ref. [47], Fourier coefficients v_1 , v_2 , and v_3 are calculated for unidentified charged hadrons within $|\eta| < 0.35$, with respect to the corresponding participant planes Ψ_1 , Ψ_2 , and Ψ_3 . These plane angles are computed for each event from the initial coordinates of nucleon participants with a Gaussian smearing of width $\sigma = 0.4$ fm.

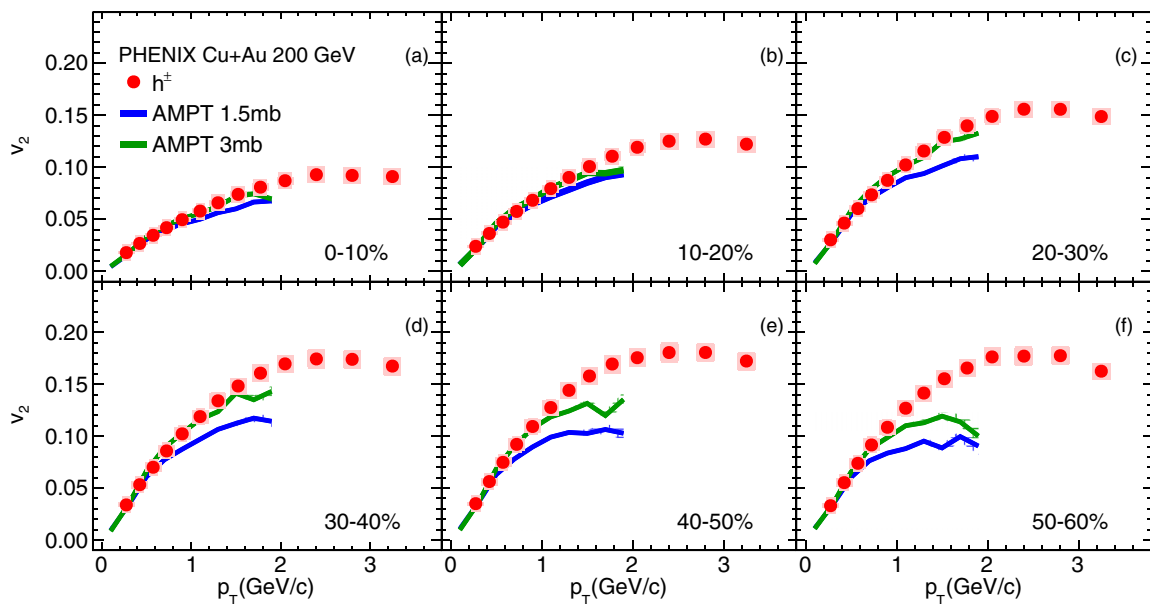


FIG. 18. The second-order Fourier coefficients $v_2(p_T)$ for charged hadrons measured at midrapidity in Cu + Au collisions at $\sqrt{s_{NN}} = 200$ GeV in comparison to AMPT model calculation for the centrality classes marked in each panel. The symbols represent the measured $v_2(p_T)$ values, the error bars show the statistical uncertainties, and the shaded boxes indicate the systematic uncertainties. For the theoretical calculations, which are shown with lines, only statistical uncertainties are plotted.

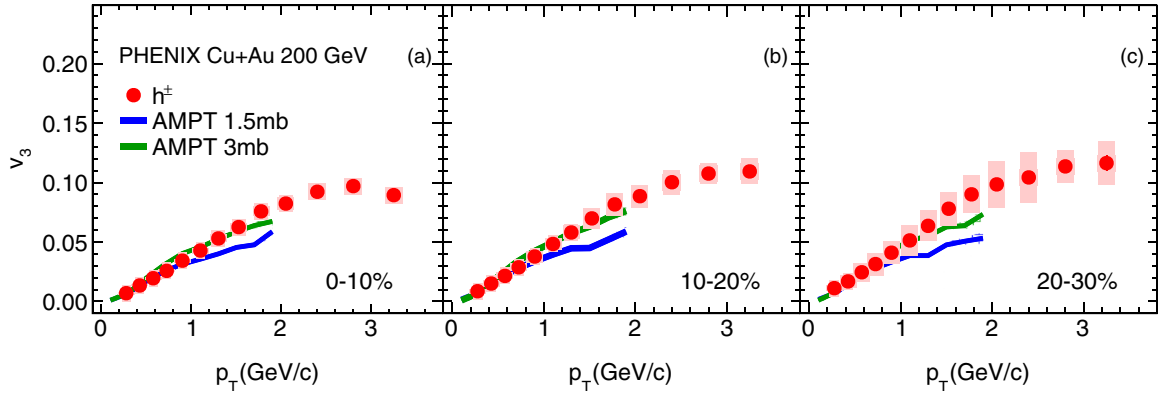


FIG. 19. The third-order Fourier coefficients $v_3(p_T)$ for charged hadrons measured at midrapidity in Cu + Au collisions at $\sqrt{s_{NN}} = 200$ GeV in comparison to AMPT model calculation for the centrality classes marked in each panel. The symbols represent the measured $v_3(p_T)$ values, the error bars show the statistical uncertainties, and the shaded boxes indicate the systematic uncertainties. For the theoretical calculations, which are shown with lines, only statistical uncertainties are plotted.

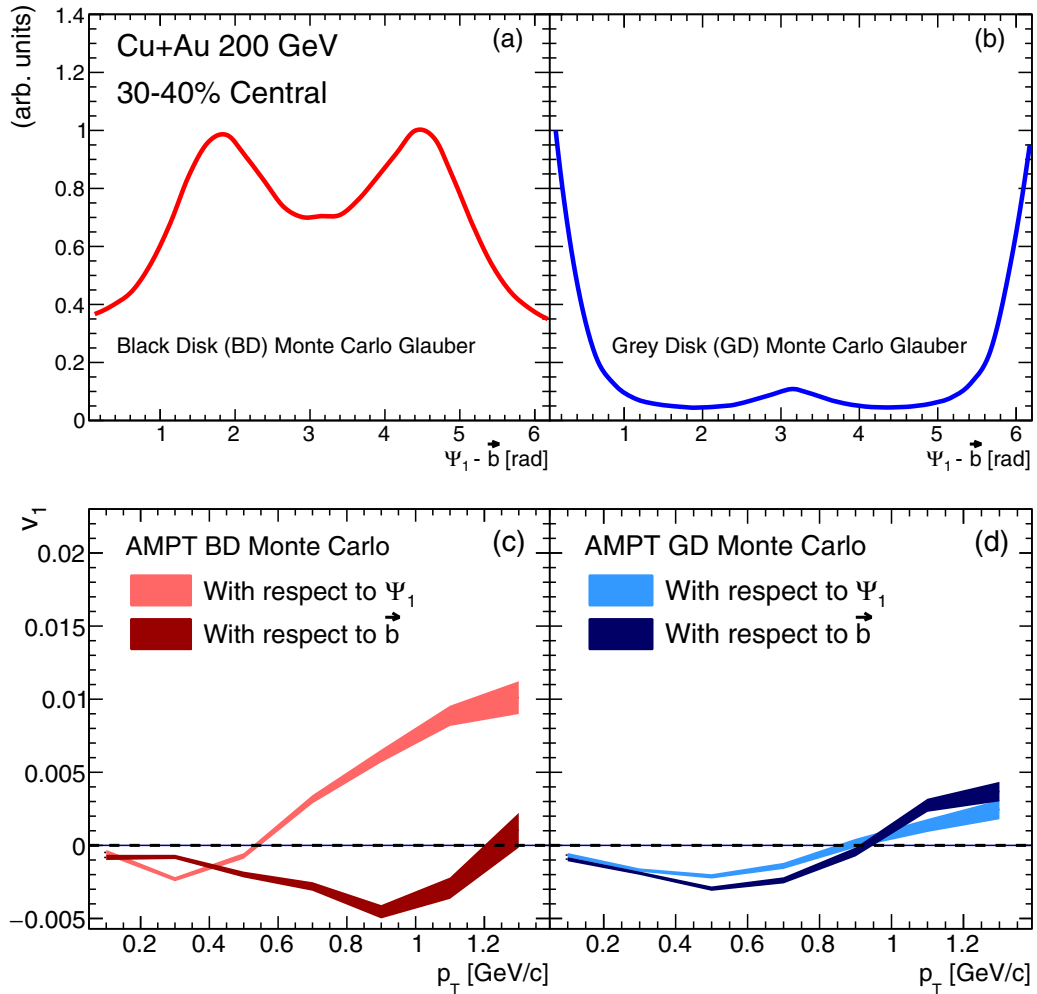


FIG. 20. The top panels show the maximum-normalized distribution of first-order participant plane angle Ψ_1 computed from the initial coordinates of participant nucleons determined with (a) black-disk, and (b) gray-disk Monte Carlo Glauber simulations. The bottom panels show AMPT v_1 computed with respect to the impact parameter \vec{b} , and Ψ_1 using (c) black-disk and (d) gray-disk Monte Carlo for the initial conditions.

The $v_2(p_T)$ and $v_3(p_T)$ results shown in Figs. 18 and 19 are well reproduced by the model for $p_T < 1$ GeV/ c . The comparison with the data indicates that the 3.0 mb partonic cross section gives a better description of the system dynamics.

However, the calculation of v_1 and its comparison with experimental data is less straightforward. Because the experimentally measured Cu spectator neutron orientation is unknown, we calculate the v_1 values with respect to the impact parameter vector \vec{b} pointing in the direction of the Cu nucleus as well as with respect to Ψ_1 , the overlap region calculated as previously described. Because the calculation is done in the participant center-of-mass frame, weighting all participants equally yields exactly $\varepsilon_1 = 0$ and hence no direction for Ψ_1 . There are various suggestions in the literature for weighting with r^2 and r^3 [48,49], and in this study we choose to use r^2 .

In addition, we have considered two different Monte Carlo Glauber initial conditions, one with black-disk (BD) nucleons and one with gray-disk (GD) nucleons, thus varying the diffuseness of the nucleon-nucleon interaction radius. Figure 20 shows results for Cu + Au collisions within the 30%-40% centrality selection on the relative distribution of Ψ_1 to \vec{b} pointing in the direction of the Cu nucleus. Figure 20(a) is for the BD case and Fig. 20(b) is for the GD case. This small difference in the treatment of initial geometry completely reorients the Ψ_1 vector. The lower panels show the AMPT midrapidity particle v_1 as a function of p_T relative to Ψ_1 and \vec{b} in the BD and GD implementations. It is interesting to note that, in the GD case where the two results agree, the prediction is for low- p_T particles moving in the direction of the Au nucleus and the high- p_T particles in the direction of the Cu nucleus (opposite to the previously discussed hydrodynamic prediction).

We note that it is currently unknown whether the spectator neutrons bend toward or away from the interaction overlap region between the nuclei, and whether they are oriented along the impact parameter vector \vec{b} , along the vector Ψ_1 determined by the initial energy density in the overlap region, or some other vector. In fact, it is conceivable that spectators very close to the overlap region have a different behavior from spectators far away from the overlap. These ambiguities need resolution before a more direct theory to data comparison can be made.

IV. SUMMARY

Anisotropic flow coefficients for inclusive charged particles and identified hadrons π^\pm , K^\pm , p , and \bar{p} produced in Cu + Au collisions at $\sqrt{s_{NN}} = 200$ GeV have been measured by the PHENIX experiment at RHIC using event-plane techniques. The v_1 , v_2 , and v_3 measurements were performed at midrapidity as a function of transverse momentum p_T over a broad range of collision centralities. Mass ordering was observed for low p_T in the identified particle measurements, as predicted by hydrodynamics.

A system size comparison was performed for the inclusive charged particles using previous PHENIX measurements at $\sqrt{s_{NN}} = 200$ GeV of $v_2(p_T)$ in Cu + Cu and Au + Au collisions, and $v_3(p_T)$ in Au + Au collisions. The elliptic and triangular flow measurements between different systems and centrality selections were found to scale with the product of the

initial participant eccentricity and the third root of the number of nucleon participants $\varepsilon_n N_{\text{part}}^{1/3}$. The system size dependence of the $v_3(p_T)$ values could also be described by participant eccentricity ε_3 scaling alone.

The inclusive charged-particle measurements were compared with theoretical predictions. In the v_1 measurement, we observed negative values at high p_T , indicating that hadrons are emitted in the transverse plane preferentially in the hemisphere of the spectators from the Au nucleus, assuming that they moved outward from the interaction region and are aligned with the impact parameter vector. The AMPT transport model calculations were found to be in agreement with the magnitude of the measured $v_1(p_T)$ signals, but having the opposite sign. At low p_T (< 1 GeV/ c), AMPT provides a reasonable description of the triangular flow in all measured centrality classes that cover the 0%-30% range, and the elliptic flow measurements in the 0%-60% range. Event-by-event hydrodynamics calculations with specific viscosity in the range $\eta/s = 0.08$ -0.16 reproduce the measured $v_2(p_T)$ and $v_3(p_T)$ values.

ACKNOWLEDGMENTS

We thank the staff of the Collider-Accelerator and Physics Departments at Brookhaven National Laboratory and the staff of the other PHENIX participating institutions for their vital contributions. We acknowledge support from the Office of Nuclear Physics in the Office of Science of the Department of Energy, the National Science Foundation, Abilene Christian University Research Council, Research Foundation of SUNY, and Dean of the College of Arts and Sciences, Vanderbilt University (USA), Ministry of Education, Culture, Sports, Science, and Technology and the Japan Society for the Promotion of Science (Japan), Conselho Nacional de Desenvolvimento Científico e Tecnológico and Fundação de Amparo à Pesquisa do Estado de São Paulo (Brazil), Natural Science Foundation of China (People's Republic of China), Croatian Science Foundation and Ministry of Science, Education, and Sports (Croatia), Ministry of Education, Youth and Sports (Czech Republic), Centre National de la Recherche Scientifique, Commissariat à l'Énergie Atomique, and Institut National de Physique Nucléaire et de Physique des Particules (France), Bundesministerium für Bildung und Forschung, Deutscher Akademischer Austausch Dienst, and Alexander von Humboldt Stiftung (Germany), National Science Fund, OTKA, Károly Róbert University College, and the Ch. Simonyi Fund (Hungary), Department of Atomic Energy and Department of Science and Technology (India), Israel Science Foundation (Israel), Basic Science Research Program through NRF of the Ministry of Education (Korea), Physics Department, Lahore University of Management Sciences (Pakistan), Ministry of Education and Science, Russian Academy of Sciences, Federal Agency of Atomic Energy (Russia), VR and Wallenberg Foundation (Sweden), the US Civilian Research and Development Foundation for the Independent States of the Former Soviet Union, the Hungarian American Enterprise Scholarship Fund, and the US-Israel Binational Science Foundation.

- [1] S. Voloshin and Y. Zhang, Flow study in relativistic nuclear collisions by Fourier expansion of azimuthal particle distributions, *Z. Phys. C: Part. Fields* **70**, 665 (1996).
- [2] K. Adcox *et al.* (PHENIX Collaboration), Formation of dense partonic matter in relativistic nucleus-nucleus collisions at RHIC: Experimental evaluation by the PHENIX collaboration, *Nucl. Phys. A* **757**, 184 (2005).
- [3] J. Adams *et al.* (STAR Collaboration), Experimental and theoretical challenges in the search for the quark gluon plasma: The STAR Collaboration's critical assessment of the evidence from RHIC collisions, *Nucl. Phys. A* **757**, 102 (2005).
- [4] B. B. Back *et al.*, The PHOBOS perspective on discoveries at RHIC, *Nucl. Phys. A* **757**, 28 (2005).
- [5] E. V. Shuryak, What RHIC experiments and theory tell us about properties of quark-gluon plasma? *Nucl. Phys. A* **750**, 64 (2005).
- [6] M. Gyulassy and L. McLerran, New forms of QCD matter discovered at RHIC, *Nucl. Phys. A* **750**, 30 (2005).
- [7] J. Barrette *et al.* (E877 Collaboration), Energy and charged particle flow in a 10.8 A/GeV/c Au + Au collisions, *Phys. Rev. C* **55**, 1420 (1997); **56**, 2336(E) (1997).
- [8] C. Alt *et al.* (NA49 Collaboration), Directed and elliptic flow of charged pions and protons in Pb + Pb collisions at 40-A GeV and 158-A-GeV, *Phys. Rev. C* **68**, 034903 (2003).
- [9] C. Adler *et al.* (STAR Collaboration), Elliptic flow from two and four particle correlations in Au + Au collisions at $\sqrt{s_{NN}} = 130$ GeV, *Phys. Rev. C* **66**, 034904 (2002).
- [10] L. Adamczyk *et al.* (STAR Collaboration), Elliptic flow of identified hadrons in Au + Au collisions at $\sqrt{s_{NN}} = 7.7$ –62.4 GeV, *Phys. Rev. C* **88**, 014902 (2013).
- [11] B. Alver *et al.* (PHOBOS Collaboration), System Size, Energy, Pseudorapidity, and Centrality Dependence of Elliptic Flow, *Phys. Rev. Lett.* **98**, 242302 (2007).
- [12] A. Adare *et al.* (PHENIX Collaboration), Systematic study of azimuthal anisotropy in Cu + Cu and Au + Au collisions at $\sqrt{s_{NN}} = 62.4$ and 200 GeV, *Phys. Rev. C* **92**, 034913 (2015).
- [13] K. Aamodt *et al.* (ALICE Collaboration), Elliptic Flow of Charged Particles in Pb-Pb Collisions at 2.76 TeV, *Phys. Rev. Lett.* **105**, 252302 (2010).
- [14] G. Aad *et al.* (ATLAS Collaboration), Measurement of the pseudorapidity and transverse momentum dependence of the elliptic flow of charged particles in lead-lead collisions at $\sqrt{s_{NN}} = 2.76$ TeV with the ATLAS detector, *Phys. Lett. B* **707**, 330 (2012).
- [15] S. Chatrchyan *et al.* (CMS Collaboration), Measurement of the elliptic anisotropy of charged particles produced in Pb-Pb collisions at $\sqrt{s_{NN}} = 2.76$ TeV, *Phys. Rev. C* **87**, 014902 (2013).
- [16] B. B. Back *et al.* (PHOBOS Collaboration), Energy Dependence of Directed Flow Over a Wide Range of Pseudorapidity in Au + Au Collisions at RHIC, *Phys. Rev. Lett.* **97**, 012301 (2006).
- [17] L. Adamczyk *et al.* (STAR Collaboration), Beam-Energy Dependence of the Directed Flow of Protons, Antiprotons, and Pions in Au + Au Collisions, *Phys. Rev. Lett.* **112**, 162301 (2014).
- [18] B. Abelev *et al.* (ALICE Collaboration), Directed Flow of Charged Particles at Midrapidity Relative to the Spectator Plane in Pb-Pb Collisions at $\sqrt{s_{NN}} = 2.76$ TeV, *Phys. Rev. Lett.* **111**, 232302 (2013).
- [19] D. H. Rischke, Horst Stoecker, W. Greiner, and B. L. Friman, Phase transition from hadron gas to quark gluon plasma: Influence of the stiffness of the nuclear equation of state, *J. Phys. G: Nucl. Phys.* **14**, 191 (1988).
- [20] B. Alver and G. Roland, Collision geometry fluctuations and triangular flow in heavy-ion collisions, *Phys. Rev. C* **81**, 054905 (2010); **82**, 039903(E) (2010).
- [21] A. Adare *et al.* (PHENIX Collaboration), Measurement of the higher-order anisotropic flow coefficients for identified hadrons in Au + Au collisions at $\sqrt{s_{NN}} = 200$ GeV, *Phys. Rev. C* **93**, 051902 (2016).
- [22] A. Adare *et al.* (PHENIX Collaboration), Measurements of Higher-Order Flow Harmonics in Au + Au Collisions at $\sqrt{s_{NN}} = 200$ GeV, *Phys. Rev. Lett.* **107**, 252301 (2011).
- [23] L. Adamczyk *et al.* (STAR Collaboration), Third harmonic flow of charged particles in Au + Au collisions at $\sqrt{s_{NN}} = 200$ GeV, *Phys. Rev. C* **88**, 014904 (2013).
- [24] K. Aamodt *et al.* (ALICE Collaboration), Higher Harmonic Anisotropic Flow Measurements of Charged Particles in Pb-Pb Collisions at $\sqrt{s_{NN}} = 2.76$ TeV, *Phys. Rev. Lett.* **107**, 032301 (2011).
- [25] G. Aad *et al.* (ATLAS Collaboration), Measurement of the azimuthal anisotropy for charged particle production in $\sqrt{s_{NN}} = 2.76$ TeV lead-lead collisions with the ATLAS detector, *Phys. Rev. C* **86**, 014907 (2012).
- [26] S. Chatrchyan *et al.* (CMS Collaboration), Measurement of higher-order harmonic azimuthal anisotropy in Pb-Pb collisions at $\sqrt{s_{NN}} = 2.76$ TeV, *Phys. Rev. C* **89**, 044906 (2014).
- [27] B. Schenke, S. Jeon, and C. Gale, Higher flow harmonics from (3+1)D event-by-event viscous hydrodynamics, *Phys. Rev. C* **85**, 024901 (2012).
- [28] Sean Gavin and G. Moschelli, Fluctuation probes of early-time correlations in nuclear collisions, *Phys. Rev. C* **85**, 014905 (2012).
- [29] L. X. Han, G. L. Ma, Y. G. Ma, X. Z. Cai, J. H. Chen, S. Zhang, and C. Zhong, Initial fluctuation effect on harmonic flow in high-energy heavy-ion collisions, *Phys. Rev. C* **84**, 064907 (2011).
- [30] G. Y. Qin, H. Petersen, S. A. Bass, and B. Muller, Translation of collision geometry fluctuations into momentum anisotropies in relativistic heavy-ion collisions, *Phys. Rev. C* **82**, 064903 (2010).
- [31] Z. Qiu and U. W. Heinz, Event-by-event shape and flow fluctuations of relativistic heavy-ion collision fireballs, *Phys. Rev. C* **84**, 024911 (2011).
- [32] P. Staig and E. Shuryak, The fate of the initial state fluctuations in heavy ion collisions. III The second act of hydrodynamics, *Phys. Rev. C* **84**, 044912 (2011).
- [33] K. Adcox *et al.* (PHENIX Collaboration), PHENIX detector overview, *Nucl. Instrum. Methods Phys. Res., Sect. A* **499**, 469 (2003).
- [34] C. Adler, A. Denisov, E. Garcia, M. Murray, H. Strobele, and S. White, The RHIC zero-degree calorimeters, *Nucl. Instrum. Methods Phys. Res., Sect. A* **499**, 433 (2003).
- [35] D. Ben-Tzvi and M. B. Sandler, A combinatorial Hough transform, *Pattern Recognit. Lett.* **11**, 167 (1990).
- [36] A. Adare *et al.* (PHENIX Collaboration), Spectra and ratios of identified particles in Au + Au and *d* + Au collisions at $\sqrt{s_{NN}} = 200$ GeV, *Phys. Rev. C* **88**, 024906 (2013).
- [37] M. Aizawa *et al.* (PHENIX Collaboration), PHENIX central arm particle ID detectors, *Nucl. Instrum. Methods Phys. Res., Sect. A* **499**, 508 (2003).
- [38] A. Adare *et al.* (PHENIX Collaboration), Deviation from quark-number scaling of the anisotropy parameter v_2 of pions, kaons,

- and protons in Au + Au collisions at $\sqrt{s_{NN}} = 200$ GeV, *Phys. Rev. C* **85**, 064914 (2012).
- [39] A. M. Poskanzer and S. A. Voloshin, Methods for analyzing anisotropic flow in relativistic nuclear collisions, *Phys. Rev. C* **58**, 1671 (1998).
- [40] M. Alvioli and M. Strikman, Beam fragmentation in heavy ion collisions with realistically correlated nuclear configurations, *Phys. Rev. C* **83**, 044905 (2011).
- [41] S. Afanasiev *et al.* (PHENIX Collaboration), Systematic studies of elliptic flow measurements in Au + Au collisions at $\sqrt{s} = 200$ GeV, *Phys. Rev. C* **80**, 024909 (2009).
- [42] S. J. Sanders M. L. Miller, K. Reygers and P. Steinberg, Glauber modeling in high-energy nuclear collisions, *Annu. Rev. Nucl. Part. Sci.* **57**, 205 (2007).
- [43] A. Adare *et al.* (PHENIX Collaboration), Scaling Properties of Azimuthal Anisotropy in Au + Au and Cu + Cu Collisions at $\sqrt{s} = 200$ GeV, *Phys. Rev. Lett.* **98**, 162301 (2007).
- [44] P. Bozek, Event-by-event viscous hydrodynamics for Cu-Au collisions at 200 GeV, *Phys. Lett. B* **717**, 287 (2012).
- [45] Z.-W. Lin, C. M. Ko, B.-A. Li, B. Zhang, and S. Pal, A multi-phase transport model for relativistic heavy ion collisions, *Phys. Rev. C* **72**, 064901 (2005).
- [46] L.-W. Chen and C. M. Ko, Anisotropic flow in Cu + Au collisions at $\sqrt{s_{NN}} = 200$ GeV, *Phys. Rev. C* **73**, 014906 (2006).
- [47] J. D. Orjuela Koop, A. Adare, D. McGlinchey, and J. L. Nagle, Azimuthal anisotropy relative to the participant plane from a multiphase transport model in central $p + Au$, $d + Au$, and ${}^3\text{He} + Au$ collisions at $\sqrt{s_{NN}} = 200$ GeV, *Phys. Rev. C* **92**, 054903 (2015).
- [48] F. G. Gardim, F. Grassi, Y. Hama, M. Luzum, and J.-Y. Ollitrault, Directed flow at mid-rapidity in event-by-event hydrodynamics, *Phys. Rev. C* **83**, 064901 (2011).
- [49] D. Teaney and L. Yan, Triangularity and dipole asymmetry in heavy ion collisions, *Phys. Rev. C* **83**, 064904 (2011).